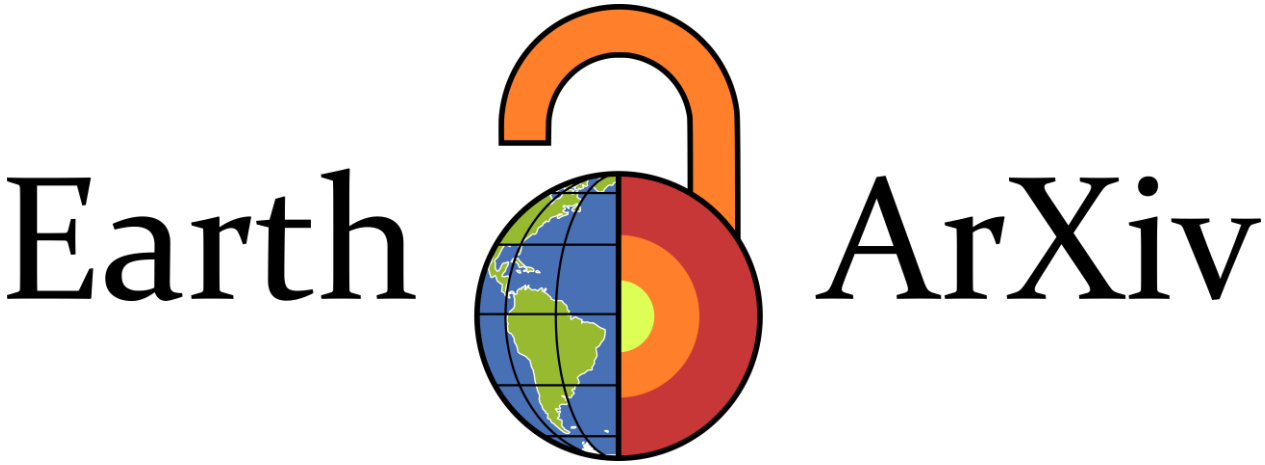

Polymineralic synneusis in silicic magmas revealed by megacryst-inclusion orientation relationships

Charlotte Gordon[1] and David Wallis[1]

[1]Department of Earth Sciences, University of Cambridge, Downing Street, Cambridge, CB2 3EQ, U.K.

Email: c.gordon@berkeley.edu; dw584@cam.ac.uk

ABSTRACT

Crystal aggregation via synneusis is well-documented in many common igneous minerals, such as quartz and olivine. Synneusis is typically described as a monomineralic process whereby two crystals of the same mineral adhere in specific low-energy orientation relationships. In contrast, unlike minerals are generally assumed to be antipathetic. Nonetheless, the occurrence of polymineralic synneusis (systematically oriented attachment of unlike mineral pairs) has been postulated but never quantitatively demonstrated. Therefore, the occurrence and characteristics of polymineralic synneusis, and its impacts on the behaviour of magmatic systems, remain poorly understood.

We apply spatially correlated microstructural analyses, including electron backscatter diffraction and cathodoluminescence mapping, to test whether polymineralic crystal aggregates can form via synneusis. The abundant mineral inclusions within K-feldspar megacrysts in granites have previously been postulated to arise from polymineralic synneusis, therefore we chose to study examples of this texture from two unrelated plutons. Textural observations confirm that inclusions of plagioclase, amphibole and various accessory minerals grew independently in the magma before attaching to the megacrysts.

Analysis of the crystallographic orientations of plagioclase, amphibole, titanite and magnetite relative to their host K-feldspar reveal variably systematic orientation relationships. Plagioclase, amphibole and titanite show distinct suites of orientations within each growth sector of the K-feldspar, while magnetite does not. Titanite orientations appear to be controlled mainly by shape, whereas amphibole orientations cannot easily be explained by shape alone, so may also have a crystallographic control. Plagioclase orientations are tightly crystallographically controlled due to the lattice similarities between K-feldspar and plagioclase. Some of the observed K-feldspar-plagioclase orientation relationships follow established feldspar twin laws, which represent low-energy grain interfaces. However, we also observe orientation relationships that have not been documented as growth twins and are diagnostic synneusis relationships. In particular, the predominance of combined Baveno-type relationships resulting from the attachment of (010) and (001) feldspar faces appears to be unique to synneusis. We infer that crystals encountering each other in the magma attached, and then rotated into more favourable orientations, due to the minimisation of interfacial energy.

Synneusis has been considered diagnostic of low-viscosity, low-crystallinity magmas, but our results demonstrate that this is not always the case, as the megacrysts grew in relatively viscous, silicic, crystal-rich magma. The occurrence of polymineralic synneusis even in these granitic systems suggests that it may be an important and widespread magmatic process, creating crystal clusters that potentially impact both the rheological behaviour and geochemical evolution of the host magma.

Keywords: (up to 5, alphabetical, separated by semicolons)

EBSD; Granite; Megacryst; Microstructure; Synneusis

INTRODUCTION

Crystal clusters are ubiquitous in igneous rocks and can be valuable archives of information about magmatic processes. Interpreting the petrological significance of crystal clusters hinges on understanding the mechanisms by which they form. A variety of cluster-forming mechanisms may operate in magma, each with distinct petrogenetic implications. Clusters and similar microstructures have been attributed to processes including heterogeneous nucleation (Kirkpatrick, 1977; Hammer *et al.*, 2010), mush disaggregation (Cashman *et al.*, 2017; Neave *et al.*, 2017), growth twinning (Dowty, 1980), resorption (Hogan, 1993), disequilibrium crystallisation (Barbee *et al.*, 2020; McCarthy *et al.*, 2020), dendrite annealing (Welsch *et al.*, 2013), and synneusis (e.g., Vance, 1969).

Synneusis is the attachment of crystals that originally grew independently in melt before converging and joining (Vogt, 1921). Vogt (1921) introduced the term with reference to monomineralic clustering, but in an influential later paper, Vance (1969) broadened the definition to include polymineralic synneusis. Vance also added the important observation that synneusis typically occurs via attachment on important crystallographic planes, and in preferred orientations defined by positions of low interfacial energy (Vance, 1969). Although some authors have since mentioned synneusis in a polymineralic context (e.g., Vernon, 2018), research on the process of synneusis, and its petrological implications, has focused on monomineralic synneusis. Detailed microstructural work has revealed evidence of monomineralic synneusis in a variety of common igneous minerals, including olivine (Schwindinger and Anderson, 1989; Wieser *et al.*, 2019), plagioclase (Vance, 1969; Bennett *et al.*, 2019), chromite (Holness *et al.*, 2023), zircon (Jocelyn and Pidgeon, 1974; Alexandrov, 2001) and quartz (Beane and Wiebe, 2012; Dyck and Holness, 2022; Dyck, 2023).

In recent years, studies of synneusis have greatly benefitted from the application of crystallographic orientation mapping by electron backscatter diffraction (EBSD). EBSD enables quantification of crystallographic orientation relationships (CORs) between adjacent crystals (Habler and Griffiths, 2017), confirming that synneusis attachments preferentially occur on significant crystallographic faces and feature characteristic CORs (e.g., Beane and Wiebe, 2012). Monomineralic synneusis clusters are characterised by coincident-site lattice relationships where the lattices of neighbouring grains are aligned to minimise the energy of the grain boundary, e.g., twin laws (Dyck and Holness, 2022; Dyck, 2023).

EBSD also introduces the potential to quantify CORs between unlike crystal pairs. Such analysis has already been applied to magmatic epitaxial relationships (Hammer *et al.*, 2010), xenocryst reaction rims (Schuster *et al.*, 2023) and inclusions in garnet (Griffiths *et al.*, 2016). Furthermore, recent EBSD analysis indicated that highly systematic CORs can result from the synneusis of K-feldspar and plagioclase in granite (Gordon and Wallis, 2024) but the sample size in that study was insufficient to allow thorough characterisation of the CORs present. Low-energy relationships in monomineralic systems are relatively straightforward to model with reference to common faces, twin laws, and coincident-site lattice modelling (Dyck and Holness, 2022), whereas polymineralic orientation relationships are more challenging to characterise and benefit from the analysis of large datasets (Griffiths *et al.*, 2016). EBSD therefore presents a gateway to studying the phenomenon of polymineralic synneusis.

At present, we know very little about whether unlike mineral pairs are “sticky” towards each other in magmas, and the default assumption is that they are antipathetic: that if two crystals of different minerals were to encounter each other in magma, there would be no significant drive for them to adhere. However, polymineralic synneusis is challenging to distinguish from other clustering mechanisms using standard petrographic or geochemical

methods, and therefore its prevalence may have been underestimated. To assess the occurrence and significance of polymineralic synneusis, a new approach is necessary. Systematic orientation relationships between unlike pairs of minerals may prove diagnostic of synneusis, even in otherwise cryptic clusters.

To develop polymineralic synneusis as a useful petrological tool, we must first define its characteristic orientation relationships and textures. We must also consider the magmatic conditions under which polymineralic synneusis occurs, so that when evidence of polymineralic synneusis is identified in the rock record, meaningful petrogenetic inferences can be made. In this paper, we aim to undertake foundational work towards these goals.

Megacrysts: ideal for characterisation of polymineralic synneusis

Oriented inclusions in K-feldspar megacrysts in granites are the quintessential microstructure thought to arise from polymineralic synneusis. Euhedral, systematically arranged inclusions of plagioclase, amphibole, biotite and other minerals are ubiquitous in alkali feldspar megacrysts (e.g., Booth, 1968; Cox *et al.*, 1996; Vernon and Paterson, 2008), and are frequently ascribed to synneusis (e.g., Hibbard, 1965; Vernon, 1986; Moore and Sisson, 2008; Gordon and Wallis, 2024). Vance (1969) commented that "K-feldspar phenocrysts with oriented plagioclase inclusions are among the most spectacular and useful of the common synneusis structures".

Megacryst inclusions also make an excellent case study because each megacryst typically contains thousands of small inclusions of a variety of minerals. Abundant small inclusions in one large host crystal are ideal for COR identification (Griffiths *et al.*, 2016), and the presence of inclusions of a range of common rock-forming minerals enables a variety of mineral-pair CORs to be characterised and compared.

The petrological significance of synneusis in granites

Synneusis is commonly thought to be confined to low-viscosity melts, in which crystals can easily move relative to each other via settling (Schwindinger and Anderson, 1989; Schwindinger, 1999; Alexandrov, 2001; Wieser *et al.*, 2019), turbulent flow (Vance, 1969) and bidirectional conduit flow (DiBenedetto *et al.*, 2020). Granites therefore seem an unlikely environment for synneusis, because even at low crystallinities they have viscosities high enough to impede turbulent flow and crystal settling (Glazner, 2014). However, synneusis in granites appears to be widespread (e.g., Beane and Wiebe, 2012; Dyck and Holness, 2022) and is not even confined to low crystallinities; Gordon and Wallis (2024) found that the synneusis of plagioclase and K-feldspar megacrysts occurs at moderate crystallinities of ~35–55% crystals.

The occurrence of synneusis in these high-viscosity, crystal-rich systems raises fundamental questions about the processes by which crystals interact and adhere to each other in magmas. Synneusis microstructures may not be reliable indicators of low crystallinity environments, or of commonly invoked processes such as settling. Therefore, the latter part of this paper discusses some possible mechanisms by which crystals may come together in silicic melts and attach in systematic orientations.

GEOLOGICAL BACKGROUND

K-feldspar megacrysts containing oriented inclusions are extremely common in silicic plutons. We chose to sample two unrelated calc-alkaline batholiths: the well-studied Tuolumne Intrusive Complex in California, and the Separation Point Granite in New Zealand.

The Tuolumne Intrusive Complex, in the Sierra Nevada batholith, comprises older (from ~95 Ma), more mafic granodiorites and tonalites around the margins, and progressively younger (to ~85 Ma) and more evolved granodiorite and granite units toward the centre

148 (Bateman and Chappell, 1979; Coleman *et al.*, 2004). We sampled the two main megacrystic
149 units of the complex: the central Cathedral Peak Granodiorite (CP) and the slightly less
150 evolved Porphyritic Half Dome Granodiorite (pHD).
151 The Separation Point Batholith (SP) is situated in the north of New Zealand's South
152 Island, and is approximately 120 km long and around 10 km wide. The batholith is mainly
153 composed of homogeneous, medium- to coarse-grained, biotite-hornblende monzogranite,
154 but also includes granodiorites (Muir *et al.*, 1995). The north of the batholith is zoned from
155 equigranular hornblende-biotite monzogranite in the west to K-feldspar megacrystic biotite
156 monzogranite in the east (Muir *et al.*, 1995), and we sampled the latter. U/Pb geochronology
157 of zircons from the Separation Point Granite yields a pooled age of 112±1.9 Ma (Bolhar *et*
158 *al.*, 2008).
159 The field characteristics of the two plutons are similar. Megacrysts are distributed
160 heterogeneously, with local concentrations interpreted as areas of physical accumulation (e.g.,
161 Vernon, 1986; Vernon and Paterson, 2008). The megacrysts are commonly aligned in a
162 magmatic fabric (Fig. 1) both in the normal bulk granite, and in outcrop-scale structures such
163 as ladder dykes and enclave swarms. Megacrysts are sometimes aligned such that their main
164 faces are flat against their neighbours' faces, but they do not impinge on one another except
165 in their anhedral overgrowth rims (Fig. 1b).
166
167 **METHODS**
168 **Sampling and sample preparation**
169 Field observations were made in both study areas to establish petrological context and
170 ensure that the samples collected were representative. We sampled ten sites across the
171 Tuolumne Intrusive Complex, and made thin sections of two megacrysts and one groundmass
172 sample per site. Where possible, the megacrysts were cut through their cores and normal to a

major face. Four representative megacrysts for large-area EBSD mapping (Fig. 2), were selected based on freshness, abundance of inclusions, and simplicity of megacryst morphologies. One of the megacrysts included in this study (Sample G) was previously described by Gordon and Wallis (2024). Sampling locations are given in Table 1.

At the Separation Point Batholith, weathered-out euhedral megacrysts are abundant in local drift deposits and we collected loose megacrysts from beaches near Kaiteriteri. Sampling loose megacrysts enabled us to identify the exterior faces of the megacrysts and cut sections through the cores. Two megacrysts were sectioned, and one was selected for large-area EBSD mapping.

Petrography and geochemistry

We examined thin sections of the megacrysts, their inclusions and the associated groundmass using transmitted light microscopy. QEMSCAN mapping was performed with a step size of 10 µm on a FEI Quanta 650 field emission gun scanning electron microscope (SEM) equipped with two energy-dispersive X-ray spectrometry (EDS) detectors. Cathodoluminescence (CL) mapping was conducted on the same SEM.

Electron backscatter diffraction

We conducted EBSD mapping of the Tuolumne megacrysts on a Zeiss Gemini 300 SEM with an Oxford Instruments Symmetry detector and Aztec 4.0 acquisition software. EBSD on the Separation Point sample was performed on a FEI Quanta 650 SEM with an Oxford Instruments Symmetry S3 detector and Aztec 6.1 acquisition software. We used apertures of 100–120 µm and accelerating voltages of 20–30 kV. Working distances were typically 23–25 mm, and patterns were collected using Speed 1 mode. The Tuolumne samples were mapped at high vacuum with a 6 nm carbon coat, and the SP sample was

mapped uncoated at low vacuum. The maps have step sizes of 10–20 µm, which are small enough to capture most plagioclase inclusions. Misindexing between K-feldspar and plagioclase was minimised by using an anorthite match unit for plagioclase, as described by Gordon and Wallis (2024). K-feldspar was indexed using an orthoclase match unit. Titanite was indexed against a match unit derived from Hawthorne *et al.*, (1991), which uses a different unit cell setting to the conventional morphological setting. We therefore converted our titanite Miller indices to the morphological setting.

We performed initial de-noising in CHANNEL5 Tango software by removing wild spikes. For maps with poor indexing, we also created filled versions of the datasets to minimise loss of inclusions with a low number of indexed pixels during the manual screening procedure outlined below.

Comparison of the EBSD maps with CL and transmitted light images revealed that a substantial number of the indexed plagioclase grains were either exsolved albite, or systematic misindexing of K-feldspar. To alleviate this issue, all plagioclase grains in each EBSD dataset were manually screened with the aid of CL and transmitted light microscopy so that only genuine inclusions were accepted into the dataset for analysis. Where plagioclase inclusions contained multiple twins, only one of each twin orientation was included in the dataset, to remove the bias towards large inclusions with polysynthetic twins. Only one twin was detected in most plagioclase grains, but this is most likely a sampling artifact, as polysynthetic twinning is visible in almost all plagioclase grains with cross-polarised transmitted light at high magnification. Therefore, the detected orientation of a given inclusion may not always represent the twin member that actually formed the attachment surface with the host crystal, but is likely related to it by a twin law, most commonly the albite or pericline law.

Further EBSD data processing was performed using MTEX version 5.10.2, an open-source toolbox for manipulating EBSD data (Bachmann *et al.*, 2010), in MATLAB R2020b. All inclusion orientations were rotated into a reference frame defined by the crystal lattice of the host megacryst (Fig. 7), enabling data from multiple megacrysts to be pooled. CL and EBSD data were used to identify the megacryst growth sector that each inclusion lay within; in other words, which face of the megacryst each inclusion interacted with during its incorporation (Fig. 2). The megacryst faces in each map were identified by comparing the zonation visible in CL to stereonet projections of the traces of possible faces modelled from the EBSD data. Data from faces that could not be identified were excluded.

Where the MTEX crystalShape function was used to visualise orientations, the crystalShape habits were customised to match as closely as possible the actual habits of each mineral in the samples.

PETROGRAPHIC AND GEOCHEMICAL RESULTS

Every megacryst studied contains abundant inclusions (Fig. 3), which are predominantly of plagioclase, although every mineral present in the groundmass except quartz also occurs as euhedral inclusions. Inclusions are concentrated in particular growth zones of the host crystal, and sometimes also in particular megacryst growth sectors. The inclusions have shape preferred orientations parallel to the euhedral form of their host megacryst. In the following sections we describe the Tuolumne megacrysts first, before providing observations of the Separation Point megacrysts for comparison.

Textures of the Tuolumne megacrysts

Megacrysts feature euhedral cores 2–10 cm long, with overgrowth rims that extend interstitially into the groundmass. The overgrowth rims are a subtly different colour in hand

specimen, and typically have finer-scale exsolution lamellae than the euhedral cores. Microcline twins, where present, tend to be coarser near grain boundaries.

The megacrysts have complex concentric zones that are broadly euhedral, with planar surfaces that can be assigned to the common growth faces of K-feldspar (Fig. 4b). Each zone is CL-bright towards the interior of the crystal, gradually darkening towards the rim, before a sharp transition back to CL-bright K-feldspar, and the repetition of the pattern. The sharp zone boundaries can be near-planar, undulating or embayed, and sometimes truncate boundaries that lie to the interior of the crystal. The gradient in CL brightness of each zone follows the topography of its underlying boundary.

Inclusions have a variety of spatial relationships to the megacryst zones, and can occur anywhere within a zone, although some zones host more inclusions than others. Euhedral inclusions almost never occur flush against a smooth planar zone boundary in the megacryst. Inclusions commonly sit in a shallow embayment in the zone boundary, where the embayment follows the shape of the inclusion (Fig. 4a, c, d). Similar shallow embayments with no visible inclusion may be associated with one lying outside the plane of view. Some inclusions sit within a zone or, less commonly, across a zone boundary with no embayment. Rarely, an inclusion sits on a segment of zone boundary that stands proud from the surrounding boundary. Horizons containing many large euhedral inclusions are generally associated with an underlying deeply incised boundary that truncates several previous zones (e.g., left hand edge of Fig. 4c).

CL also reveals the presence of complex embayments with irregular linear or branching shapes that have no relationship to the normal growth zones (e.g. Fig 4f). These deep embayments sometimes contain inclusions with atypical orientations. The embayments contain CL-dark K-feldspar, which is sometimes finely banded parallel to the embayment margins, with cross-cutting relationships indicating inwards growth. Some embayments are

fracture-like in form with CL-uniform interiors, while those with complex fine bands tend to be smooth-edged and wider. There is never any visible offset across the embayments. The cores of the embayments are often quartz (Fig. 4f), which is usually unzoned but occasionally features contact-parallel zones. Neighbouring embayments sometimes contain seemingly separate cores of quartz that are in crystallographic continuity with each other and are most likely interconnected outside the plane of view. Similar quartz patches surrounded by CL-dark K-feldspar occur in association with some inclusions, especially filling the gaps between crystals in clusters (Fig. 3).

Plagioclase inclusions

The Tuolumne plagioclase inclusions are texturally diverse. Some are large (up to ~4 mm long) and euhedral, but there are also abundant smaller inclusions, many of which are anhedral. Zonation that is visible in cross-polarised light is more common in the larger inclusions. Inclusions commonly have a ragged rim of albite that is in optical continuity with neighbouring perthitic albite lamellae. EDS confirms that the zoned plagioclase inclusions have more calcic cores and more sodic rims, as well as irregular albite rims (Fig. 4e). Elongate euhedral inclusions usually have their long axes oriented approximately parallel to the zones/face of the host. Where plagioclase inclusions occur in contact with each other, they often have parallel or twinned relationships with their neighbours.

Large, euhedral plagioclase inclusions are generally more common towards the outside of the megacryst, or sometimes in a distinct growth horizon within the megacryst, associated with a deeply incised zone boundary. Relatively planar zone boundaries are occasionally followed by abundant small anhedral plagioclase inclusions.

In CL, the plagioclase inclusions sometimes feature clear concentric euhedral zones, especially in the larger inclusions (Fig. 4d). The zonation patterns of large euhedral inclusions

297 in the outer parts of the megacryst sometimes match those of the groundmass plagioclase.
298 Some plagioclase inclusions, especially those that are small and anhedral, have fine-scale
299 complex zones. Plagioclase inclusions within any given growth zone of a megacryst can have
300 a wide variation in their own internal zonation patterns.
301
302 **Quartz inclusions**
303 Quartz inclusions are common in the Tuolumne megacrysts and can be up to
304 approximately 3mm long. The inclusions are anhedral, usually blobby or elongate, and
305 usually associated with the cores of complex embayments. Linear inclusions feature tapering
306 protrusions into the surrounding K-feldspar. Seemingly separate but neighbouring quartz
307 inclusions often enter extinction simultaneously. Euhedral inclusions of quartz are extremely
308 rare and only occur at the margins of megacrysts.
309
310 **Inclusions of other phases**
311 All of the megacrysts contain accessory minerals, but mafic minerals are more
312 abundant in the megacrysts of the less evolved pHD than they are in the CP megacrysts.
313 Amphibole inclusions are typically < 1.5 mm long and euhedral. Euhedral zones are
314 sometimes visible in cross-polarised light, and simple twins are common (Fig. 5). Amphibole
315 sometimes occurs in small clusters with parallel faces (Fig. 5) and often occurs alongside
316 magnetite. Amphibole inclusions are commonly oriented with their long axes roughly parallel
317 to the host face. While some amphiboles appear to have a face parallel to that of the K-
318 feldspar host, others do not (Fig. 5).
319 Biotite is rarely included in the megacrysts despite being common in the groundmass.
320 Where biotite inclusions occur, they tend to be clustered with other mafic minerals. Isolated

biotite inclusions are typically oriented with their cleavage parallel to the trace of the face of the host, and are most abundant near the megacryst rims.

Various accessory minerals are present in the megacrysts. Titanite occurs as euhedral diamond or kite shaped crystals, usually < 1mm long, with complex concentric zones visible in BSE images. Titanite inclusions typically have a long axis or major face parallel to the trace of the host face. Equant, subhedral magnetite crystals occur both as solitary inclusions, and in clusters of mafic minerals. Apatite crystals are typically euhedral, and often occur in clusters with mafic inclusions.

K-feldspar inclusions in the K-feldspar megacrysts are extremely rare. CL occasionally hints at the presence of a K-feldspar inclusion with an orientation the same as that of its host, and one thin section contains an inclusion with an orientation different to that of its host, which will be discussed below.

Groundmass textures

The groundmass crystals are generally much larger than inclusions of the same phase, and this effect is especially pronounced for plagioclase. The groundmass plagioclase features complex oscillatory zonation and often occurs in clusters of several plagioclase crystals that appear to have systematic orientation relationships.

Quartz is an interstitial phase in the groundmass, although its internal zonation sometimes records an early stage of euhedral growth. Sometimes the zones also contain smoothed non-euhedral boundaries suggestive of resorption. No irregularly shaped dendritic or embayed zone morphologies were observed.

The K-feldspar in the groundmass is unzoned, both in cross-polarised light and CL, and is interstitial between groundmass crystals of plagioclase. Groundmass K-feldspar is often a crystallographically continuous overgrowth of a nearby megacryst. Non-megacrystic

346 groundmass crystals do occur, but are indistinguishable from megacryst overgrowths in CL
347 images. In at least one case (Sample I), the orientation of the contact between the groundmass
348 K-feldspar originating as a megacryst overgrowth and the independent groundmass K-
349 feldspar is defined by the crystallography of the latter, with the groundmass crystal therefore
350 appearing to predate the megacryst overgrowth. In most other cases, the groundmass crystals
351 are anhedral and have irregular contacts with other K-feldspar groundmass crystals.
352 Exsolution lamellae are less well developed in the groundmass K-feldspar than in the
353 megacrysts.
354 The mafic and accessory minerals in the groundmass are euhedral to subhedral, and
355 larger than their counterparts included within the megacrysts. Mafic minerals typically occur
356 in clusters, and most apatite is included within biotite or amphibole, sometimes in apparently
357 systematic orientations.
358
359 **Petrography of the Separation Point megacrysts**
360 The SP samples are texturally similar to those from Tuolumne. The megacrysts are
361 perthitic, with coarser exsolution lamellae in their cores than their rims, and microcline twins
362 that coarsen near the albite lamellae. The inclusions are concentrically arranged and have a
363 strong shape preferred orientation parallel to the faces of the host megacryst. The inclusion
364 assemblage comprises mostly plagioclase, with rare euhedral titanite and equant iron oxides.
365 Altered polycrystalline biotite and chlorite occasionally appear to have pseudomorphed
366 amphibole. Albite rims on plagioclase inclusions are rarer in the SP megacrysts than those
367 from Tuolumne but are sometimes present. As with the Tuolumne megacrysts, the SP
368 megacrysts lack euhedral quartz inclusions but feature elongate slug-like quartz inclusions.

369 The groundmass comprises plagioclase, quartz, alkali feldspar and biotite, with
370 accessory iron oxides and apatite. Undulose extinction in the quartz and kinks in the biotite
371 record mild deformation.
372
373 **EBSD RESULTS**
374 This section describes the habits, faces and twins of the minerals of interest, then
375 presents the orientation distributions of the inclusions. Particular attention is given to
376 plagioclase, which has the most complex orientation relationships with the host.
377
378 **Crystal habits and twins**
379 The megacrysts from both batholiths have prominent (010) and (001) faces with
380 smaller {110} and ($\bar{2}$01) faces. Simple twins are common, but we chose to avoid them for the
381 EBSD maps, except in sample G which contains four twin members related by Baveno and
382 Manebach laws (Fig. 2).
383 The plagioclase crystals have habits with large (010) and (001) faces, and are
384 ubiquitously twinned, most commonly on the albite, Carlsbad, albite-Carlsbad, pericline, and
385 Ala laws. The amphibole crystals are elongate along [001], with prominent {110} faces and
386 smaller or absent (010) and (100) faces. The titanite crystals have prominent {111} faces and
387 occasionally also show minor faces including (100) and (001).
388
389 **3D axis-angle plotting to check for crystallographic orientation relationships**
390 Plotting the host-inclusion data in axis-angle space allows a rapid qualitative
391 assessment of whether any systematic CORs are present in the data, in a way that inherently
392 accounts for the symmetry mismatch between different minerals (Fig. 6). We pooled the
393 inclusion data from all of the EBSD datasets, and plotted the misorientations between the K-

feldspar and the inclusion minerals following the methods of Krakow et al. (2017). Misorientations between crystals are plotted in a 3D vector space, where the magnitude of the vector (the distance from the origin) corresponds to the misorientation angle (ω), and the direction corresponds to the misorientation axis in a common reference frame where [001] of every mineral lies along z and (100)* lies along x. The shape of the 3D fundamental region required to plot the data is determined by symmetry, for which Krakow et al. (2017) provide details. We coloured each datum according to the megacryst growth sector in which the inclusion is located.

In the plots, tight clusters of points correspond to specific CORs. A radial line of points indicates that crystals are related by continuous rotation about a specific axis. Loose clusters indicate that the misorientations are non-random but contain scatter in both axis and angle of misorientation.

The plagioclase misorientations are highly organised, with at least 14 specific CORs (Fig. 6a, b). Even data outside these CORs are preferentially arrayed along particular radial lines (indicating preferred misorientation axes) and at particular distances from the origin (indicating preferred misorientation angles). Some CORs are only present within particular growth sectors of the host plagioclase.

Titanite and amphibole both display moderately organised misorientation data (Fig. 6c–f). No strong specific CORs are present, but the misorientation data are not randomly distributed. In both minerals, inclusions from each megacryst sector cluster loosely together.

Magnetite misorientations are poorly organised (Fig. 6g, h). The few linear arrangements that appear in axis-angle space (e.g., projected over the origin in Fig. 6h) comprise < 5 points, and a much larger dataset would be required to assess whether they are significant, therefore we do not discuss them further.

General statement on the plagioclase inclusion orientations

EBSD reveals that the orientations of the plagioclase inclusions are strongly systematic in every sample. The megacryst growth sectors associated with each major face contain distinctive suites of associated plagioclase orientations (Fig. 8). Orientation systematics in each megacryst sector were consistent across all samples from both batholiths. In the following plots, we have therefore pooled data from all Tuolumne megacrysts into one set of pole figures. Data from the SP sample, which had (010) and (001) growth sectors, are presented separately for comparison.

As established by Gordon and Wallis (2024), crystals that lie in the groundmass beyond the euhedrally zoned portion of the megacrysts have random orientations, even though many of them are in contact with interstitial K-feldspar that is in crystallographic continuity with the megacrysts. We found the same to be true in the samples of this study, therefore inclusions situated beyond the euhedrally zoned portions of the megacrysts were excluded from all further analysis.

In the remainder of this paper, Miller indices have a subscript with a mineral abbreviation where there could be ambiguity about which mineral they concern, e.g., $(010)_{Kfs}$ refers to (010) planes of K-feldspar, while $(010)_{Pl}$ refers to (010) planes of plagioclase. Where statements apply to both minerals, or the context is unambiguous, no subscript is used. All pole figures are plotted in the standard K-feldspar reference frame defined in Fig. 6. Pole figures are lower hemisphere unless otherwise specified.

Plagioclase inclusions in megacryst (010) growth sectors

The plagioclase inclusions hosted within $(010)_{Kfs}$ growth sectors have systematic orientations. In the $(010)^*_{Pl}$ pole figures (Fig. 9), the data cluster tightly around the location of $(010)^*_{Kfs}$, demonstrating that the (010) planes of the two minerals are often parallel. As

[010] and (010)* are near-parallel in plagioclase, the distributions of $[010]_{Pl}$ and $(010)^*_{Pl}$ match closely, but the clustering of $(010)^*_{Pl}$ is slightly tighter.

$(001)^*_{Pl}$ data form three main clusters. One cluster is parallel to $(010)^*_{Kfs}$, and a pair of clusters are located where $(001)^*_{Pl}$ poles are situated ~25° to either side of $[001]_{Kfs}$ within the $(010)_{Kfs}$ plane. Most $[001]_{Pl}$ axes lie within the $(010)_{Kfs}$ plane, mainly clustered around $[001]_{Kfs}$ but also in two smaller clusters approximately 60° to either side. $[001]_{Pl}$ axes also occur within a small circle ~25° away from $(010)^*_{Kfs}$.

$[100]_{Pl}$ are almost all concentrated within the $(010)_{Kfs}$ plane, mostly in two major clusters ~65° to either side of $[001]_{Kfs}$, with a third cluster parallel to $[001]_{Kfs}$.

Plagioclase inclusions in megacryst (001) growth sectors

Plagioclase inclusion orientations in the $(001)_{Kfs}$ growth sector are also highly systematic (Fig. 10). In contrast to the large single cluster of $(010)^*_{Pl}$ in the $(010)_{Kfs}$ sector, in the $(001)_{Kfs}$ sector there are two main clusters of $(010)^*_{Pl}$, with a weaker one parallel to $(010)^*_{Kfs}$ and a stronger one parallel to $(001)^*_{Kfs}$. There is also a slight concentration of $(010)^*_{Pl}$ within the $(001)_{Kfs}$ plane. The $[010]_{Pl}$ axes have a very similar distribution, but with weaker clustering.

$(001)^*_{Pl}$ are tightly clustered parallel to $(001)^*_{Kfs}$. Weaker concentrations of $(001)^*_{Pl}$ lie approximately within the $(001)_{Kfs}$ plane, at $(010)^*_{Kfs}$ and ~55° to either side of it. $[001]_{Pl}$ clusters around $[001]_{Kfs}$, especially in the Tuolumne data, with some spread around a small circle ~25° away from $(001)^*_{Kfs}$. $[001]_{Pl}$ are also distributed within the $(001)_{Kfs}$ plane, in two stronger clusters ~30° to either side of $[010]_{Kfs}$ and a weaker, more elongate cluster ~90° away from $[010]_{Kfs}$.

$[100]_{Pl}$ lie mostly within the $(001)_{Kfs}$ plane, in a main cluster parallel to $[100]_{Kfs}$ and two weaker clusters ~65° to either side.

Plagioclase inclusions in megacryst ($\bar{2}01$) growth sectors

$(010)^*_{Pl}$ cluster parallel to $(\bar{2}01)^*_{Kfs}$ (Fig. 11), with a second weaker cluster parallel to $(010)^*_{Kfs}$. The $[010]_{Pl}$ axes feature two clusters, one parallel to $[010]_{Kfs}$ and one at $(\bar{2}01)^*_{Kfs}$.

$(001)^*_{Pl}$ are also strongly clustered parallel to $(\bar{2}01)^*_{Kfs}$, with a weak cluster parallel to $(001)^*_{Kfs}$. The $[001]_{Pl}$ axes are relatively scattered, but feature a small cluster parallel to $[001]_{Kfs}$, a weak girdle within the $(\bar{2}01)_{Kfs}$ plane, and a weak concentration within a small circle ~25° away from $(\bar{2}01)^*_{Kfs}$. $[100]_{Pl}$ axes are oriented either parallel to $[100]_{Kfs}$ or within the $(\bar{2}01)_{Kfs}$ plane.

Amphibole inclusions

Only our $(001)_{Kfs}$ and $(\bar{2}01)_{Kfs}$ megacryst growth sectors yielded substantial amphibole data. The amphibole orientation distributions are different in these two sectors (Fig. 12). In both sectors, $[001]_{Hb}$ axes form an uneven girdle within the plane of the host face, while $[100]_{Hb}$ axes cluster normal to the host face. In the $(\bar{2}01)_{Kfs}$ sector, $[001]_{Hb}$ are clustered parallel to $[010]_{Kfs}$. The $(100)^*_{Hb}$ clusters are stronger than the $[100]_{Hb}$ clusters in both growth sectors. The $(010)^*_{Hb}$ distributions are scattered. $\{110\}^*_{Hb}$ directions in both growth sectors form a loose cluster around the pole to the host face.

Titanite inclusions

As with amphibole, titanite inclusions have distinctive orientation distributions in each megacryst growth sector (Fig. 13). Inclusions in $(010)_{Kfs}$ growth sectors feature a cluster of $\{111\}^*_{Ttn}$ parallel to $(010)^*_{Kfs}$, while those in $(001)_{Kfs}$ growth sectors have $\{111\}^*_{Ttn}$ clustered parallel to $(001)^*_{Kfs}$. Both growth sectors also feature minor clusters of $(100)^*_{Ttn}$ parallel to the pole to the host face.

K-feldspar inclusion

There is one example in the EBSD datasets where a megacryst includes a smaller K-feldspar grain with an orientation distinct from that of the host (Fig. 14). The grain is hosted within the (001) sector of Sample B and is ~0.7 mm long, with irregular patchy zonation in CL (Fig. 14). The (001) face of the inclusion is parallel to that of the host, and its [100] axis is very close to that of the host, but the [001] axis of the inclusion is not aligned with that of the host. The host-inclusion orientation relationship is ~9° away from an ideal Manebach twin relationship.

ANALYSIS OF MICROSTRUCTURES AND ORIENTATION RELATIONSHIPS

Growth of inclusions prior to incorporation

As synneusis is the attachment of crystals that formed separately in magma (Vance 1969), the first step in identifying synneusis structures is to establish whether the crystals involved nucleated independently. Heterogeneous nucleation of one crystal on another could produce similar textures (Dowty, 1980), including CORs (e.g., Hammer *et al.,* 2010).

In the case of inclusions in K-feldspar megacrysts, there is strong evidence for independent nucleation and growth prior to attachment. Inclusions of all phases except quartz are commonly euhedral, indicating growth in free space unimpeded by neighbouring crystals. Many inclusions contain complete, concentric, symmetrical zones, further evidencing growth surrounded by melt (Fig. 4a, d). Plagioclase inclusions within a given megacryst horizon can feature diverse zonation patterns in CL, suggesting that they grew in separate environments to each other before coming together.

Sectioning effects can theoretically result in the appearance of concentric zonation in a crystal that had nucleated heterogeneously on a surface (Dowty 1980). However, in the present dataset this effect can be ruled out in most cases, as the orientations of both the host

519 and the inclusion faces are known. None of the inclusions analysed exhibit the asymmetrical
520 zones expected from heterogeneous nucleation on the surface of the megacryst.
521 There are many examples where the plagioclase crystals are anhedral, with no visible
522 zonation or complex non-concentric zonation, perhaps due to episodes of resorption. It is
523 possible, though not required, that some of these small anhedral crystals nucleated on the
524 megacryst. However, the euhedral inclusions unequivocally formed separately to the
525 megacryst, and euhedral, subhedral and anhedral inclusions commonly occur alongside each
526 other within any given growth zone of a megacryst and display the same CORs with the host
527 (Fig. 8). Therefore, it is most likely that the anhedral inclusions also formed independently in
528 the melt, but experienced resorption prior to attachment. This interpretation is consistent with
529 the extensive evidence of resorption in the megacryst zonation.
530
531 **The role of planar faces**
532 It is typically assumed that crystals attach by synneusis when their large, flat faces
533 come into contact. Such a model could adequately explain the titanite orientation
534 distributions, where a major face such as {111} or (100) is commonly parallel to the
535 megacryst face to which the inclusion attached. Some amphiboles have a large {110} face
536 parallel to the host face. Most plagioclase inclusions have either (001) or (010) parallel to the
537 host face, and because (001) and (010) are commonly large crystal faces in feldspars, this
538 parallelism could arise when two euhedral crystals meet on their major faces.
539 However, the joining of planar faces is not an entirely satisfactory explanation for the
540 CORs. Both the megacrysts and the inclusions frequently do not have planar faces, even
541 when their orientation relationships are systematic. The megacryst zones feature rounded
542 corners, wavy boundaries and embayments, and many of the inclusions are subhedral or
543 anhedral. In addition, even inclusions with large, planar faces are not always in a perfect

544 COR with the host crystal. Just like anhedral crystals, the euhedral crystals sometimes have
545 imperfect or random orientations. Crystals therefore appear to attach to each other with
546 systematic CORs independently of having large, flat faces.
547 Figure 15 illustrates modelled axes distributions for feldspar-feldspar attachments if the
548 only constraint were alignment of the (001) and (010) faces. We model the inclusion as
549 monoclinic for simplicity, but triclinic, albite-twinned plagioclase would result in some of the
550 lines splitting into two parallel lines separated by a few degrees, an effect that contributes to
551 apparent scatter in the observed data. The figure illustrates that a geometric control on
552 orientation due solely to the meeting of crystal faces would generate smooth girdles.
553 Although there is some resemblance between the model (Fig. 15) and the data (Fig. 9 and
554 10), importantly, the axes in the data cluster strongly within the predicted girdles.
555 In summary, the presence of planar faces is not required for synneusis to occur, and
556 attachment on planar faces alone cannot account for all characteristics of the data. The
557 inclusion orientations therefore appear to be controlled at least in part by lattice effects and
558 the minimisation of interfacial energies.
559
560 **Feldspar twin laws control plagioclase inclusion orientations**
561 Previous researchers have disagreed about whether plagioclase inclusions in K-feldspar
562 display crystallographic preferred orientations, or simply shape preferred orientations.
563 Several early studies suggested crystallographic alignments (Vance, 1969 and references
564 therein). However, Dowty (1980) reported that “in most cases there is no systematic
565 crystallographic alignment other than parallelism of the faces; and the only face of
566 attachment of the plagioclase seems to be (010)”. The latter point is not consistent with our
567 data, as the plagioclase inclusions also routinely attach to megacrysts on $(001)_{Pl}$ (Fig. 9, 10

568 and 11). We will now address the former claim that there is no systematic crystallographic
569 alignment.
570 The crystal axes of the inclusions exhibit strong clustering (Fig. 9, 10) within the
571 girdles allowed by parallel alignment of faces (Fig. 15), strongly suggesting a
572 crystallographic control on the orientations of the inclusions. In this section, we will
573 demonstrate that the orientation clusters can be explained by the interplay of three influences:
574 the identities of the host and inclusion attachment planes, twinning within included
575 plagioclase grains, and the attachment of plagioclase to K-feldspar in specific preferred
576 orientations. We will discuss each of the common feldspar twin laws to explain how they
577 underpin the clusters in the orientation data. The identified feldspar orientation relationships
578 are summarised schematically in Fig. 17.
579 In the pole figures we follow the convention for triclinic minerals and present
580 plagioclase axis data without antipodal symmetry, although the megacryst reference frame
581 and the plagioclase polysynthetic twinning effectively symmetrise the $[100]_{Pl}$ and $[001]_{Pl}$ data
582 such that every cluster in the upper hemisphere has a lower-hemisphere counterpart. For
583 simplicity, the modelled twin orientations in Fig. 16 are illustrated using orthoclase lattice
584 parameters and antipodal symmetry. Plagioclase lattice parameters would result in some
585 lattice directions being a few degrees away from the modelled orientations, but the
586 fundamental findings are unaffected.
587
588 *Albite and pericline*
589 Albite and pericline twin laws (180° about (010)* and [010] respectively) are
590 symmetrically invalid for monoclinic feldspars, but occur as polysynthetic twins within the
591 included plagioclases. Therefore, some of the data clusters comprise two sub-clusters

592 separated by a few degrees, due to albite/pericline twins superimposed on the other
593 orientation relationships described below.
594
595 *Parallel attachment*
596 Parallel attachment is the lowest energy orientation for the joining of two crystals of the
597 same mineral by synneusis, and is normally by far the most common (Vance, 1969). The data
598 are consistent with this statement also being true for synneusis between plagioclase and K-
599 feldspar; the strongest clusters in the plagioclase pole figures are typically parallel to the
600 same crystal direction in the host megacryst. In the Tuolumne data from the (001) growth
601 sector (Fig. 10), $[010]_{Pl}$ are skewed to the upper hemisphere, parallel to $[010]_{Kfs,}$ instead of
602 $[0\bar{1}0]_{Kfs}$ which lies in the lower hemisphere of our reference frame, suggesting a preference
603 for parallel alignment. The $(\bar{2}01)_{Kfs}$ sectors are an exception, perhaps because it is
604 unfavourable for plagioclase crystals to attach to K-feldspar on $(\bar{2}01)_{Pl}$ as would be required
605 to facilitate parallelism. Plagioclase usually attaches on $(010)_{Pl}$ or $(001)_{Pl}$ even on $(\bar{2}01)_{Kfs}$.
606
607 *Manebach and Ala*
608 The Manebach law involves a 180° rotation about (001)* while the Ala laws involve
609 180° rotations about [100]. The laws result in the same orientation relationship in monoclinic
610 feldspars, which we will henceforth refer to as the Manebach relationship for simplicity. An
611 inclusion attaching to a megacryst with a Manebach relationship would have $(010)_{Pl}$ and
612 $(001)_{Pl}$ parallel to those of the megacryst, regardless of whether it attached to $(010)_{Kfs}$ or
613 $(001)_{Kfs}$ (Fig. 16). Manebach relationships may therefore be likely synneusis relationships for
614 meetings of both $(001)_{Pl}$ on $(001)_{Kfs}$, and $(010)_{Pl}$ on $(010)_{Kfs}$
615 The Manebach law leaves the [100] and [010] axes parallel to their original positions
616 but results in a ~52° anticlockwise offset of $[001]_{Pl}$ in our reference frame (Fig. 16). There is

617 elevated data density here (Fig. 9, 10), but it is not very pronounced. Consider a meeting of
618 $(001)_{Pl}$ and $(001)_{Kfs}$. A 26° circle of possible positions is available to $[001]_{Pl}$ but in most cases
619 the inclusion attaches with $[001]_{Pl}$ parallel to $[001]_{Kfs}$. More rarely, it may attach in a
620 Manebach relationship, and more rarely still, in a random orientation within the restriction of
621 parallelism of $(001)_{Pl}$ and $(001)_{Kfs}$. Likewise, in the $(010)_{Kfs}$ sectors $[001]_{Pl}$ are usually
622 parallel to $[001]_{Kfs}$ and more rarely in a Manebach position. Manebach attachments are
623 therefore possible, but rare.
624
625 *Carlsbad and X law*
626 The Carlsbad law involves a rotation of 180° around [001], and the X law is a 180°
627 rotation around (100)* (Fig. 16). As before, the two laws have the same outcome for
628 monoclinic feldspars, which we will refer to as a Carlsbad relationship. A Carlsbad
629 relationship brings neither $(001)_{Pl}$ nor $(010)_{Pl}$ parallel to $(001)_{Kfs}$, therefore we expect no
630 Carlsbad attachments to $(001)_{Kfs}$, and indeed the data exhibit no elevated occurrence of
631 Carlsbad relationships (Fig. 10). In contrast, the Carlsbad relationship is very common in the
632 $(010)_{Kfs}$ data, as evidenced by the $[100]_{Pl}$ clusters that are offset by ~56° clockwise from
633 $[100]_{Kfs}$ (Fig. 9). The relationship is favourable in the $(010)_{Kfs}$ growth sector because a
634 Carlsbad relationship would bring $(010)_{Pl}$ parallel to $(010)_{Kfs}$.
635
636 *Baveno*
637 The Baveno laws merit particular attention. They involve a 180° rotation around (021)*
638 for the Baveno right law, and $(0\bar{2}1)$* for the Baveno left law; the composition plane in alkali
639 feldspars is typically (021) or $(0\bar{2}1)$ respectively. For the feldspars in this study, Baveno
640 relationships effectively bring (010) of one twin parallel to (001) of the other twin (Fig. 16)

and can be visualised as 90° rotations around [100]. Baveno twins are rare in plagioclase (Deer *et al.*, 2013).

Because (010) and (001) are commonly large faces in plagioclase, it has repeatedly been hypothesised that synneusis of plagioclase should involve meetings on these faces, producing Baveno-like twins with distinctive (010) on (001) composition planes that would not be expected to result from growth processes (Vance, 1969; Dowty, 1980). Indeed, Dowty (1980) used the scarcity of such relationships to argue that synneusis is rare or non-existent in plagioclase. However, in the megacrysts, Baveno relationships between the host and its inclusions are very common.

Plagioclase inclusions attaching to $(001)_{Kfs}$ on $(010)_{Pl}$ geometrically cannot have their [001] or [010] axes aligned, but can align their [100] axes in a Baveno relationship, and the data show that this is common (Fig. 10). The two $[001]_{Pl}$ clusters within the $(001)_{Kfs}$ plane (Fig. 10) match the expected Baveno positions (Fig. 16). The Baveno relationship also results in $(001)^*_{Pl}$ clustering parallel to $(010)^*_{Kfs}$ even though in this sector, inclusions are not in contact with the megacryst (010) face (Fig. 10).

Plagioclase inclusions attaching to $(010)_{Kfs}$ on $(001)_{Pl}$ also geometrically cannot have their [001] or [010] axes aligned, but can align their [100] axes in a Baveno relationship. This relationship would manifest as clustering of the $[001]_{Pl}$ axes in particular positions within the 26° small circle around (001)* of the megacryst (Fig. 16), which is evident in the data (Fig. 9). In the lower hemisphere of the SP data, there are four clusters within the 26° small circle and the lower-left and upper-right of these result from the two Baveno laws. The other two clusters will be discussed in the next section. Baveno relationships should also produce an incidental cluster of $(010)^*_{Pl}$ parallel to $(001)^*_{Kfs}$, and this cluster is present in the data (Fig. 9). We can conclude that the Baveno relationship is a favourable relationship both for inclusions attaching to $(001)_{Kfs}$ on $(010)_{Pl}$, and for those attaching to $(010)_{Kfs}$ on $(001)_{Pl}$.

Combined Baveno and Carlsbad relationships

Some of the clusters in the data cannot be explained by the operation of a single twin law, but can be explained by combined twin laws. In the $(001)_{Kfs}$ growth sector data (Fig. 10), there are prominent clusters of $[100]_{Pl}$ and $(001)^*_{Pl}$ that are consistent with attachment of inclusions on their $(010)_{Pl}$ faces (Fig. 10), but are not consistent with Baveno laws (Fig. 16). These orientations can be reproduced by applying a Baveno rotation followed by a Carlsbad rotation (Fig. 16, column 3).

In the $(010)_{Kfs}$ growth sector (Fig. 9), there are similarly unexplained clusters, both within the 26° small circle of $[001]_{Pl}$, and in the $[010]_{Pl}$ data clockwise from $[001]_{Kfs}$ (Fig. 9). We can reproduce these clusters from a Carlsbad rotation followed by a Baveno rotation (Fig. 16, column 2).

The abundance of combined twin relationships in the data prompt the question of whether such relationships arise due to the attachment of plagioclase inclusions with internal Carlsbad or Baveno twins. This mechanism is unlikely for two reasons: firstly, that Baveno twins are rare in plagioclase (Deer *et al.*, 2013); and secondly, that attachment of internally twinned plagioclase fails to explain why Carlsbad-Baveno relationships are dominant within the $(010)_{Kfs}$ sector while Baveno-Carlsbad relationships dominate the $(001)_{Kfs}$ data. In contrast, if the relationships result from the attachment of individual crystals, a simple explanation emerges: Carlsbad-Baveno relationships result in a $(001)_{Pl}$ plane parallel to $(010)_{Kfs}$ but no major plane parallel to $(001)_{Kfs}$ and therefore are only viable synneusis relationships in the $(010)_{Kfs}$ growth sectors. Likewise, a Baveno-Carlsbad relationship produces $(010)_{Pl}$ parallel to $(001)_{Kfs}$ and is therefore viable for the $(001)_{Kfs}$ growth sectors, but produces no plane parallel to $(010)_{Kfs}$ so would be non-viable for $(010)_{Kfs}$ growth sectors. The combined relationships are therefore genuine synneusis relationships between the megacryst

690 and its inclusions. This conclusion is notable because combined Baveno and Carlsbad
691 relationships have not been reported as growth twins, so may be diagnostic of synneusis.
692
693 *Three-law relationships*
694 Only a few minor clusters in the plagioclase orientation distributions of the $(010)_{Kfs}$ and
695 $(001)_{Kfs}$ growth sectors remain unexplained. These remaining clusters can be reproduced by
696 applying three successive rotations away from the megacryst orientation. Three-law
697 relationships have not, to our knowledge, been reported as growth twins and are probably
698 unique to synneusis scenarios. There is no inherent reason why a combination of three twin
699 law rotations should result in a low-energy orientation relationship, therefore the only
700 relationships considered here are those suggested by the data.
701 In the $(010)_{Kfs}$ sector (Fig. 9), there is small $[001]_{Pl}$ cluster 56° clockwise of $[001]_{Kfs}$,
702 seen most clearly in the Tuolumne data, that remains unexplained. The cluster can be
703 reproduced by a Carlsbad rotation followed by two Baveno rotations (either right then left, or
704 left then right; the outcome is the same), producing an orientation with $(010)_{Pl}$ parallel to
705 $(010)_{Kfs}$ but with a distinctive $[001]_{Pl}$ position (Fig. 16, column 4).
706 In the $(001)_{Kfs}$ sector, the situation is more complex. There are two $(010)_{Pl}$ clusters
707 within the $(001)_{Kfs}$ plane, offset by 56° either side of $[010]_{Kfs}$ (Fig. 10). These clusters require
708 a Baveno rotation, then a Carlsbad rotation, then a second Baveno rotation. There are four
709 viable combinations to explain the clusters: Baveno left-Carlsbad-Baveno right, Baveno left-
710 Carlsbad-Baveno left, Baveno right-Carlsbad-Baveno right, and Baveno right-Carlsbad-
711 Baveno left. All these combinations produce orientations with $(001)_{Pl}$ parallel to $(001)_{Kfs}$ (Fig.
712 16, column 4) and are therefore viable synneusis relationships within the $(001)_{Kfs}$ growth
713 sector. Further evidence of these relationships is present in the 26° small circles formed by

714 $[001]_{Pl}$, in which a pair of faint clusters (Fig. 10; clearest in the Tuolumne data, upper
715 hemisphere) correspond to the modelled Baveno-Carlsbad-Baveno orientations (Fig. 16).
716
717 *Attachments where no twin law is geometrically viable*
718 For an inclusion attaching to the megacryst $(\bar{2}01)_{Kfs}$ face on $(010)_{Pl}$ or $(001)_{Pl}$, there are
719 no viable twin laws. The inclusion may achieve parallelism with the host by attaching on
720 $(\bar{2}01)_{Pl}$, which some inclusions do, but many inclusions instead attach on their more
721 prominent planes (Fig. 11). It is geometrically possible for an inclusion attaching to $(\bar{2}01)_{Kfs}$
722 on its $(001)_{Pl}$ to have $[010]_{Pl}$ parallel to $[010]_{Kfs}$ and the inclusions display a strong preference
723 for this relationship within the available girdle (Fig. 16). This propensity suggests that
724 synneusis pairs prefer specific low-energy orientations even where no twin laws are
725 geometrically viable.
726
727 **Imperfect attachment of a K-feldspar inclusion**
728 Only one candidate inclusion of K-feldspar was found, in Sample B (Fig. 14),
729 suggesting that small K-feldspar crystals did not frequently attach to larger ones by
730 synneusis. However, there may be sample bias as we avoided irregularly shaped megacrysts
731 that may have resulted from synneusis of K-feldspar crystals.
732 Monomineralic crystal clusters can potentially arise from growth twinning (Dowty
733 1980) but in the particular case of the inclusion in Sample B, given the apparent size
734 difference between host and inclusion, the position of the inclusion, the zonation textures and
735 the morphology of their contact, it seems unlikely that they are the product of a twinned
736 nucleus. The orientation relationship between the two grains is approximately 9° away from a
737 Manebach twin (Fig. 14). Given that both crystals are the same mineral, a growth twin would

738 be expected to obey the twin law perfectly (unlike the near-twins typical of plagioclase and
739 K-feldspar pairs, where perfect alignment is not possible).
740 Heterogeneous nucleation cannot be ruled out by the zonation, which is irregular in CL
741 (Fig. 14), but nucleation of a crystal on a substrate of the same mineral, known as
742 homoepitaxy, typically involves perfect parallel alignment (Holness *et al.*, 2023). Nucleation
743 in an orientation misaligned from a twin relationship by 9° would be energetically
744 unfavourable.
745 It is therefore more likely that the inclusion attached by synneusis in an imperfect
746 orientation, reminiscent of the imperfect synneusis attachments observed by Dyck (2023) in
747 quartz. The forces driving the inclusion into a perfect orientation may not have been able to
748 act to completion prior to overgrowth and engulfment by the host. Engulfment prior to
749 perfect alignment could also account for some of the scatter in the plagioclase orientation
750 distributions.
751 One interesting feature revealed by CL is that the included K-feldspar grain has a neck-
752 like structure visible in the zones of the host crystal (Fig. 14), as though during an episode of
753 resorption it stood proud of the surface of the host on a small pedestal. The inclusion also has
754 a rounded morphology, with truncation of its internal irregular zones. The presence of a
755 rounded shape paired with a neck is consistent with the model of Dyck (2023) in which
756 synneusis attachment occurs by paired neck growth and grain rotation. In that model, the
757 material to form the neck is scavenged from the surfaces of the crystals, which rounds off the
758 crystal surfaces (Dyck, 2023). The rounded shape of the inclusion is also consistent with a
759 dissolution-reprecipitation ripening process, whereby larger grains grow at the expense of
760 smaller grains (Mills and Glazner, 2013). Such a process could perhaps explain why the small
761 grain was overgrown by the larger one, rather than both grains continuing to grow at an equal
762 rate, if the large grain was stable and growing while the smaller one was dissolving.

763 **Amphibole orientations**

764 The amphibole pole figures (Fig. 12) do not feature clusters as tight as those found in
765 the plagioclase data, although systematic relationships are still present. The weaker
766 relationships are consistent with the fact that amphibole does not have as much in common
767 with the K-feldspar crystal structure as does plagioclase. Another likely source of scatter is
768 that amphibole frequently occurs in crystal clusters, both within the megacrysts and in the
769 groundmass. Such clusters appear to have formed prior to incorporation into the megacryst
770 (e.g., the cluster top centre of Fig. 5). As only part of each cluster could have come into
771 contact with the megacryst surface, some of the amphibole orientations present in the dataset
772 will not represent direct synneusis relationships with the host megacryst.

773 The amphibole inclusions are typically euhedral and elongate along [001], and [001]
774 commonly lies within the plane of the host face onto which they attached (Fig. 12). It is
775 tempting to interpret this as the product of simple magmatic flow alignment, but in the
776 $(\bar{2}01)_{Kfs}$ sector the amphibole [001] axes cluster around $[010]_{Kfs}$ (Fig. 12). $[010]_{Kfs}$ is
777 geometrically the shortest axis of the feldspars in this study, in common with most feldspars.
778 The fact that the longest axes of the amphiboles are aligned with the shortest axes of the K-
779 feldspars is not readily reconcilable with an origin from flow alignment alone.

780 The amphibole crystals have prominent (110) and $(1\bar{1}0)$ faces, which are related by
781 symmetry and are plotted together in the pole figures. This consideration is important for the
782 interpretation of the apparently dispersed clusters of {110}* in the pole figures. Any
783 amphibole crystal attaching to the megacryst on its (110) face has a related $(1\bar{1}0)$ face with a
784 pole that plots ~60° away from that of the attachment plane, and vice versa. Both {110}*
785 poles are included in the pole figure, contributing to the apparent dispersion (Fig. 12).
786 Nonetheless, both EBSD and petrographic observations confirm that amphiboles do
787 sometimes attach on their {110} faces. The attachment is generally imperfect, as

788 demonstrated by the breadth of the {110}* clusters parallel to each of the poles of the
789 megacryst attachment faces.
790 Both EBSD data and petrographic observations suggest that the amphiboles also
791 commonly attach on their (100) planes, which form small and poorly developed faces (Fig. 5)
792 that are often rounded off or absent altogether. It is unexpected for the crystals to attach on
793 these small, irregular faces instead of the much larger and flatter {110} faces. A possible
794 explanation for this phenomenon can be found by returning to the idea that synneusis in
795 favourable orientation relationships occurs to minimise surface energies. Large planar faces
796 are typically slow-growing and stable, whereas small faces are faster-growing and less stable.
797 It is therefore conceivable that in some cases, the greatest energy minimisation may be
798 achieved via attachment of a higher-energy smaller face. Another, related option is that the
799 rounded-off corners, in place of the (100) planes, are molecularly rough surfaces with a
800 greater spatial density of free bonds and greater potential to bond to the megacryst surface.
801
802 **Titanite orientations**
803 Titanite orientations are relatively systematic, and can be adequately explained by
804 geometrical effects whereby the large planar titanite faces come into parallelism with the host
805 face prior to engulfment. There is no particular evidence to suggest further rotation due to the
806 minimisation of interfacial energies. This lack of rotation may be because titanite and K-
807 feldspar simply have very different lattices, where rotation does not result in large energy
808 savings. Alternatively, the low-energy positions may be incompatible with the typical {111}-
809 dominated habit of titanite, which is ubiquitous in our samples. The most significant
810 crystallographic directions and features (e.g., the TiO_6 octahedra chains) do not lie within the
811 {111} faces and so no amount of rotation around {111}* will bring them into parallelism with
812 crystallographic features of the host face.

Magnetite orientations

Magnetite inclusions that have precipitated in feldspars have previously been reported to display extremely systematic orientation relationships with their host crystals, due to the alignment of features between the two lattices in low-energy orientations (e.g., Ageeva *et al.*, 2020). While existing research focuses on plagioclase, similar low-energy orientation relationships between K-feldspar and magnetite almost certainly exist. However, we found no evidence of specific CORs between magnetite and K-feldspar.

There may simply not be a large enough energetic difference between systematic and random attachment of magnetite to result in a measurable preferred orientation relationship in the context of synneusis. Magnetite grains also tend to be equant, so are not prone to shape alignment in the same way as titanite. The magnetite inclusions also commonly occur spatially clustered with amphibole and other minerals, which may have arrived at the K-feldspar surface already in a fixed configuration.

INTERPRETED PROCESSES

Synneusis requires several steps: the independent nucleation and growth of crystals; processes to bring the crystals together; and processes to attach the crystals together in the orientations that we have observed. We have established that the crystals initially grew independently; we will now discuss crystal convergence, attachment and rotation mechanisms.

Crystal convergence

Independently formed crystals must come together in order to attach by synneusis, so synneusis is commonly considered diagnostic of relatively low-viscosity magma through which crystals can easily move, for example due to settling (e.g., Vance, 1969; Jocelyn and

838 Pidgeon, 1974). However, since K-feldspar megacrysts grow in viscous, silicic magmas at
839 moderate crystallinities (Gordon and Wallis, 2024) it is worth critically assessing whether
840 significant differential motion of crystals is necessary, or whether the oriented inclusions
841 could arise from the re-orientation and incorporation of neighbouring crystals encountered by
842 the growing megacryst in a quiescent, effectively static magma.
843 Phase equilibria modelling suggests that the magma was ~35–55% crystalline during
844 megacryst growth (Gordon and Wallis, 2024), but the megacrysts only contain ~10%
845 inclusions by volume, therefore not all crystals encountered by the growing megacryst were
846 incorporated. Rejection from the megacryst appears to be insensitive to mineralogy: the
847 magma at the time would have comprised ~30–40% plagioclase and <5% mafic and
848 accessory minerals, with little or no quartz, consistent with the relative abundances of the
849 minerals as inclusions. There is no textural evidence of haloes of rejected crystals around the
850 megacrysts, therefore some crystals must have been transported away by moving magma.
851 Megacryst growth in a flowing magma is therefore required; this is consistent with field
852 observations of megacrysts showing alignment with magmatic fabrics and evidence of
853 physical accumulation (e.g., Vernon, 1986; Paterson *et al.*, 2005). A variety of processes
854 likely contributed to the magmatic flow over the lifetime of the megacryst, including magma
855 replenishment, convection, and tectonic stress.
856
857 **Mechanisms of crystal attachment**
858 While magma flow processes could bring crystals together and align neighbouring
859 crystals by shape, some further mechanism is required to account for the observed strongly
860 crystallographic orientation relationships.
861 One possibility is that crystals that serendipitously encounter a megacryst in low-energy
862 configurations are likely to adhere, while unfavourably oriented crystals do not adhere and

863 are transported away by magmatic flow. A second possibility is that unfavourably oriented
864 inclusions are rejected at the megacryst growth front and "pushed" out of the way or rotated
865 into favourable alignments by the force of crystallisation of the megacryst. A third possibility
866 is that inclusions initially attach in imperfect orientations, then rotate due to the minimisation
867 of surface energies.

868 The first two options do not fit well with the observation that megacrysts incorporate
869 crystals of every available mineral, even those that lack strongly favourable CORs and are
870 incorporated in essentially random orientations, such as magnetite. We consider it to be more
871 likely that inclusions of all minerals initially attached to the megacryst in random or weakly
872 systematic orientations controlled by crystal shape and magma flow conditions. Then, due to
873 its crystallographic similarities to the megacryst, plagioclase experienced a strong energetic
874 drive to rotate into crystallographically-controlled orientations.

875

876 **Rotation due to minimisation of interfacial energies**

877 There has been little research on rotation driven by interfacial energy in silicates.
878 However, rotation of neighbouring crystals into low-energy orientations has been directly
879 observed in partially molten alloys, where measurable rotation occurs on timescales of
880 minutes (Dake *et al.*, 2016). Rotation of silicates in magma may be slower, but rotation must
881 occur rapidly relative to megacryst growth as most plagioclase inclusions attained favourable
882 orientations before engulfment.

883 Although most plagioclase inclusions lie in preferred orientations, some do not (e.g.,
884 Fig. 8). The imperfect inclusions are not concentrated in particular growth zones (Fig. 8), so a
885 dependence on the growth rate of the megacryst is doubtful. Perhaps a more likely
886 explanation is that at the moderate, fluctuating crystallinities relevant to megacryst growth,
887 ephemeral force chains (Bergantz *et al.*, 2017) occasionally prevented free rotation.

888 **Periodicity of synneusis**

889 Inclusions are more abundant in some concentric zones than in others (Fig. 3).
890 Statistically, synneusis should occur more frequently with increasing crystallinity (Dowty,
891 1980), until the point at which crystals inhibit free movement of their neighbours (Gordon
892 and Wallis, 2024). Fluctuating crystallinity over time may therefore have exerted some
893 control over the rate of synneusis. Megacryst growth rate may also influence the ratio of
894 inclusions incorporated to crystals rejected, a phenomenon recognised in other crystalline
895 materials including ice (Yemmou *et al.*, 1991).

896 Episodic attachment of crystals could also have occurred due to variable crystal
897 mobility associated with magma replenishment (Moore and Sisson, 2008). Magma
898 replenishment could promote synneusis by mechanically perturbing the magma and
899 decreasing magma viscosity. The inclusions do not always lie on zone boundaries (see Fig. 4)
900 but the most inclusion-rich zones are typically associated with deeply incised resorption
901 horizons (Fig. 4c), suggesting high rates of synneusis are associated with episodes of
902 resorption.

903

904 **Resorption and regrowth**

905 Evidence of repeated resorption is ubiquitous in K-feldspar megacrysts. Rhythmic
906 barium zonation and resorption boundaries in megacrysts have previously been attributed to
907 magma replenishment (Słaby *et al.*, 2007; Moore and Sisson, 2008), and analogous textures
908 in anorthoclase megacrysts from Mount Erebus have been ascribed to convection
909 (Moussallam *et al.*, 2015). In the few degrees above the eutectic, K-feldspar undergoes
910 greater changes in modal abundance with temperature than other minerals (Gordon and
911 Wallis, 2024) and therefore small fluctuations in conditions cause greater resorption of K-
912 feldspar than other minerals. Prolonged magma storage buffered at or just above eutectic

913 temperatures therefore creates ideal conditions for the dissolution and reprecipitation of K-
914 feldspar. The resultant coarsening (Mills and Glazner, 2013) is a likely contributor to the
915 megacrysts' exceptional size compared to the other minerals present.
916 CL maps of the megacrysts reveal two broad categories of megacryst embayments. The
917 first type comprises deep linear or branching embayments, sometimes with zones that record
918 inwards growth of K-feldspar, culminating in a core of quartz (Fig. 4f). The embayments
919 morphologically resemble glassy melt inclusions observed in anorthoclase megacrysts from
920 Mount Erebus in Antarctica (Moussallam et al., 2015) and quartz inclusions in some rapakivi
921 granites (Vernon, 2016). The embayments appear to result from infilling of voids within the
922 megacryst, which formed both via resorption and/or reaction along weaknesses and fractures,
923 and due to the disruption of megacryst growth by inclusions.
924 The second type of embayment comprises shallower cup-shaped embayments typically
925 containing inclusions (Fig. 4a, c, d). Given that these embayments closely follow the
926 boundaries of the inclusions, we interpret them as having formed by preferential dissolution
927 along grain boundaries during resorption events. Where shallow embayments have no visible
928 inclusion, the inclusion may be out of plane or may have detached following grain-boundary
929 dissolution. Dissolution on grain boundaries during magma recharge, or "defrosting" of
930 mush, has previously been recognised in similar plutonic rocks (Barnes and Werts, 2022).
931 The presence of mineral impurities on the megacryst surface likely promotes embayment
932 formation instead of smooth or faceted resorption.
933 Resorption may promote the attachment of crystals to form monomineralic clusters, by
934 creating a localised boundary layer with a composition similar to that of the dissolving
935 crystals, that facilitates attachment (Hogan, 1993). A similar mechanism could operate during
936 the oriented attachment of plagioclase and K-feldspar.
937

Why do megacrysts have so many inclusions?

K-feldspar megacrysts are unusually rich in inclusions compared to other minerals (Fig. 3). K-feldspar stabilises at ~35% crystallinity in a typical granodiorite (Whitney, 1988; Gordon and Wallis, 2024), and megacrysts grow from nucleation to full size within a small temperature range, over which most other minerals do not undergo as large a change in modal abundance (Gordon and Wallis, 2024). Upon encountering a small crystal, the megacryst will therefore overgrow it, rather than vice versa. The dearth of asymmetrical zones in the inclusions confirms that inclusion growth was negligible during the interval between attachment and engulfment. K-feldspar's propensity for dissolution may also promote synneusis, by creating localised reactive boundary layers and energetically unfavourable irregular surfaces.

While quartz also stabilises late, it crystallises many small crystals instead of a few large ones, making it less likely to engulf its neighbours. K-feldspar also has a more diverse interface chemistry than quartz, perhaps offering greater opportunities to form the bonds necessary for synneusis. Research into quartz-neighbour relationships may provide further insight.

WIDER IMPLICATIONS

Universality of synneusis orientation relationships

Oriented inclusions are a ubiquitous feature of K-feldspar megacrysts, and the similarity between the data from Tuolumne and Separation Point (Fig. 9, 10) demonstrates that the processes governing inclusion attachment are fundamental. Magmatic conditions enhance or inhibit the frequency of synneusis attachments, but do not define the crystallographic orientation relationships.

962 The strength and distinctiveness of the CORs between K-feldspar and plagioclase (Fig.
963 17) could facilitate identification of synneusis in non-megacrystic silicic rocks. Particularly
964 promising is the finding that many common synneusis CORs are distinct from the common
965 feldspar growth twins. Baveno-type CORs with (010)/(001) composition planes and the
966 various Baveno-Carlsbad CORs are distinctive relationships that could signal synneusis even
967 where other evidence is inconclusive. The same synneusis CORs may also occur in
968 plagioclase, and further research into plagioclase glomerocryst orientation relationships
969 would be valuable.
970
971 **Synneusis at high crystallinity**
972 Synneusis has previously been considered characteristic of low-crystallinity magmas
973 (e.g., Schwindinger and Anderson, 1989; Dyck and Holness, 2022). However, synneusis of
974 megacryst inclusions occurred at moderate crystallinities (Gordon and Wallis, 2024), in a
975 magma where viscosity would have been high and the effects of crystal inertia negligible
976 (Glazner, 2014). Synneusis clusters are robust petrological evidence of an environment where
977 relative motion of crystals could occur, but are not necessarily evidence of turbulence, low
978 crystallinity, or low viscosity.
979
980 **Magma rheology and mush structure**
981 Magma is commonly envisaged as a melt with individual crystals in suspension, but
982 crystals are reactive and we have demonstrated that K-feldspar will attach to neighbours of
983 any mineralogy. Clustering of crystals via synneusis may have profound knock-on effects for
984 the structure, rheology and eruptibility of the magma (Jerram, 2003). If magmas' crystal
985 cargoes comprise irregularly shaped interlocking solid clumps, rather than individual crystals,
986 then this may, for example, increase mush permeability and stabilise melt extraction

pathways. Models concerning the physical behaviour of magma may be improved by considering the presence of irregularly shaped crystal clusters.

Identifying polymineralic synneusis in the geological record

While synneusis in megacrysts produces visibly systematic microstructures, polymineralic synneusis in other contexts may generate cryptic textures, where EBSD could prove invaluable for identifying CORs. Polymineralic synneusis CORs likely exist between many common rock-forming minerals, and once the CORs are identified, thin sections can be surveyed with EBSD to search for evidence of synneusis. Mineral pairs with specific low-energy epitaxial CORs, such as clinopyroxene and magnetite (Feinberg *et al.*, 2004; Hammer *et al.*, 2010; Peres *et al.*, 2024) and clinopyroxene and orthopyroxene (Tarney, 1969; Nicholls and Stout, 1997) may be particularly likely to form synneusis CORs. Contextualising CORs with careful microstructural characterisation to differentiate between cluster-forming processes is therefore essential.

CONCLUSIONS

The mineral inclusions in K-feldspar megacrysts attached by polymineralic synneusis. Inclusions of all minerals present in the melt were incorporated into the megacrysts, in orientations initially controlled mainly by shape. Where low-energy orientation relationships were available, the inclusions rotated into them. Plagioclase, being very similar to K-feldspar, displays extremely systematic crystallographically-controlled orientations; amphibole and titanite display weakly systematic orientations; and magnetite inclusions are not systematically oriented.

Plagioclase and K-feldspar form a distinctive suite of orientation relationships. Some relationships reflect feldspar twin laws, while others are distinctive synneusis relationships.

Baveno-like relationships with (010)/(001) attachment interfaces are extremely common, and may be characteristic of synneusis. Amphibole forms weaker orientation relationships with K-feldspar, but the relationships cannot readily be explained by geometry-controlled attachment so may also be crystallographically controlled. Titanite and magnetite inclusions do not display crystallographically-controlled orientation relationships with K-feldspar, but titanite has such an anisotropic habit that its geometry-controlled attachment results in characteristic orientation relationships within each megacryst growth sector.

Similar synneusis attachments are likely to be common in igneous rocks, but may be challenging to identify outside of megacrysts. Careful assessment of both orientation relationships and textural features (e.g., zonation patterns) is necessary to discern between synneusis and other cluster-forming processes. EBSD provides emerging opportunities to identify intracrystalline interaction processes including polymineralic synneusis in igneous rocks of any mineralogy.

FUNDING

This work was supported by the Natural Environment Research Council [NE/S007164/1 to CG] and a UK Research and Innovation Future Leaders Fellowship [grant number MR/V021788/1] to DW.

DATA AVAILABILITY STATEMENT

All data have been submitted to GFZ Data Services under the title “Microstructural and EBSD data from mineral inclusions in K-feldspar megacrysts”. The DOI is pending and will be provided at the revision stage.

ACKNOWLEDGEMENTS

We thank I. Buisman, G. Lampronti and R. Danisi for assistance with the SEM analyses carried out in the Department of Earth Sciences, University of Cambridge. The fieldwork and sampling for this study was facilitated by R. Baxter, M. Holness, S. Paterson, V. Memeti, K. Ardill, A. Wesley and the US National Park Service.

REFERENCES

Ageeva, O., Bian, G., Habler, G., Pertsev, A. & Abart, R. (2020). Crystallographic and shape orientations of magnetite micro-inclusions in plagioclase. *Contributions to Mineralogy and Petrology* **175**, 95.

Alexandrov, P. (2001). Synneusis of zircon: why not? *Mineralogical Magazine* **65**, 71–79.

Bachmann, F., Hielscher, R. & Schaeben, H. (2010). Texture Analysis with MTEX – Free and Open Source Software Toolbox. *Solid State Phenomena* **160**, 63–68.

Barbee, O., Chesner, C. & Deering, C. (2020). Quartz crystals in Toba rhyolites show textures symptomatic of rapid crystallization. *American Mineralogist* **105**, 194–226.

Barnes, C. G. & Werts, K. (2022). Magma Defrosting: Evidence from Plutonic Rocks. *Journal of Petrology* **63**, egac112.

Bateman, P. C. & Chappell, B. W. (1979). Crystallization, fractionation, and solidification of the Tuolumne Intrusive Series, Yosemite National Park, California. *Geological Society of America Bulletin* **90**, 465.

Beane, R. & Wiebe, R. A. (2012). Origin of quartz clusters in Vinalhaven granite and porphyry, coastal Maine. *Contributions to Mineralogy and Petrology* **163**, 1069–1082.

Bennett, E. N., Lissenberg, C. J. & Cashman, K. V. (2019). The significance of plagioclase textures in mid-ocean ridge basalt (Gakkel Ridge, Arctic Ocean). *Contributions to Mineralogy and Petrology* **174**, 49.

Bergantz, G. W., Schleicher, J. M. & Burgisser, A. (2017). On the kinematics and dynamics of crystal-rich systems. *Journal of Geophysical Research: Solid Earth* **122**, 6131–6159.

Bolhar, R., Weaver, S. D., Palin, J. M., Cole, J. W. & Paterson, L. A. (2008). Systematics of zircon crystallisation in the Cretaceous Separation Point Suite, New Zealand, using U/Pb isotopes, REE and Ti geothermometry. *Contributions to Mineralogy and Petrology* **156**, 133–160.

Booth, B. (1968). Petrogenetic Significance of Alkali Feldspar Megacrysts and their Inclusions in Cornubian Granites. *Nature* **217**, 1036–1038.

Cashman, K. V., Sparks, R. S. J. & Blundy, J. D. (2017). Vertically extensive and unstable magmatic systems: A unified view of igneous processes. *Science* **355**, eaag3055.

Coleman, D. S., Gray, W. & Glazner, A. F. (2004). Rethinking the emplacement and evolution of zoned plutons: Geochronologic evidence for incremental assembly of the Tuolumne Intrusive Suite, California. *Geology* **32**, 433.

Cox, R. A., Dempster, T. J., Bell, B. R. & Rogers, G. (1996). Crystallization of the Shap Granite: evidence from zoned K-feldspar megacrysts. *Journal of the Geological Society* **153**, 625–635.

Dake, J. M., Oddershede, J., Sørensen, H. O., Werz, T., Shatto, J. C., Uesugi, K., Schmidt, S. & Krill, C. E. (2016). Direct observation of grain rotations during coarsening of a semisolid Al–Cu alloy. *Proceedings of the National Academy of Sciences* **113**.

Deer, W. A., Howie, R. A. & Zussman, J. (2013). *An Introduction to the Rock-Forming Minerals*. .

DiBenedetto, M., Qin, Z. & Suckale, J. (2020). Crystal aggregates record the pre-eruptive flow field in the volcanic conduit at Kīlauea, Hawaii. *Science Advances* **6**, eabd4850.

Dowty, E. (1980). Synneusis Reconsidered. *Contributions to Mineralogy and Petrology* **74**, 75–84.

Dyck, B. (2023). Sticking together: Mechanisms of quartz synneusis in high-silica magma. *Geoscience Frontiers* **14**, 101512.

Dyck, B. & Holness, M. (2022). Microstructural evidence for convection in high-silica granite. *Geology* **50**, 295–299.

Feinberg, J. M., Wenk, H.-R., Renne, P. R. & Scott, G. R. (2004). Epitaxial relationships of clinopyroxene-hosted magnetite determined using electron backscatter diffraction (EBSD) technique. *American Mineralogist* **89**, 462–466.

Glazner, A. F. (2014). Magmatic life at low Reynolds number. *Geology* **42**, 935–938.

Gordon, C. & Wallis, D. (2024). Resolving the “megacryst paradox”: Feldspar orientation relationships record crystal mobility in granites. *Geology* **52**, 712–716.

Griffiths, T. A., Habler, G. & Abart, R. (2016). Crystallographic orientation relationships in host–inclusion systems: New insights from large EBSD data sets. *American Mineralogist* **101**, 690–705.

Habler, G. & Griffiths, T. (2017). Crystallographic orientation relationships. In: Heinrich, W. & Abart, R. (eds) *Mineral reaction kinetics: Microstructures, textures, chemical and isotopic signatures*. Mineralogical Society of Great Britain & Ireland, 541–585.

Hammer, J. E., Sharp, T. G. & Wessel, P. (2010). Heterogeneous nucleation and epitaxial crystal growth of magmatic minerals. *Geology* **38**, 367–370.

1106 Hawthorne, F. C. *et al.* (1991). Alpha-decay damage in titanite. *American Mineralogist* **76**,
1107 370–396.

1108 Hibbard, M. J. (1965). Origin of some feldspar phenocrysts and their bearing on petrogenesis.
1109 *American Journal of Science* **263**, 245–261.

1110 Hogan, J. P. (1993). Monomineralic Glomerocrysts: Textural Evidence for Mineral
1111 Resorption during Crystallization of Igneous Rocks. *The Journal of Geology*. The
1112 University of Chicago Press **101**, 531–540.

1113 Holness, M. B., Vukmanovic, Z. & O'Driscoll, B. (2023). The Formation of Chromite Chains
1114 and Clusters in Igneous Rocks. *Journal of Petrology* **64**, egac124.

1115 Jerram, D. A. (2003). Quantifying the Building Blocks of Igneous Rocks: Are Clustered
1116 Crystal Frameworks the Foundation? *Journal of Petrology* **44**, 2033–2051.

1117 Jocelyn, J. & Pidgeon, R. T. (1974). Examples of twinning and parallel growth in zircons
1118 from some Precambrian granites and gneisses. *Mineralogical Magazine* **39**, 587–594.

1119 Kirkpatrick, R. J. (1977). Nucleation and growth of plagioclase, Makaopuhi and Alae lava
1120 lakes, Kilauea Volcano, Hawaii. *Geological Society of America Bulletin* **88**, 78.

1121 Krakow, R. *et al.* (2017). On three-dimensional misorientation spaces. *Proceedings of the*
1122 *Royal Society A: Mathematical, Physical and Engineering Sciences* **473**, 20170274.

1123 McCarthy, A., Chelle-Michou, C., Blundy, J. D., Vonlanthen, P., Meibom, A. & Escrig, S.
1124 (2020). Taking the pulse of volcanic eruptions using plagioclase glomerocrysts. *Earth*
1125 *and Planetary Science Letters* **552**, 116596.

1126 Mills, R. D. & Glazner, A. F. (2013). Experimental study on the effects of temperature
1127 cycling on coarsening of plagioclase and olivine in an alkali basalt. *Contributions to*
1128 *Mineralogy and Petrology* **166**, 97–111.

1129 Moore, J. G. & Sisson, T. W. (2008). Igneous phenocrystic origin of K-feldspar megacrysts in
1130 granitic rocks from the Sierra Nevada batholith. *Geosphere* **4**, 387.

1131 Moussallam, Y. *et al.* (2015). Megacrystals track magma convection between reservoir and
1132 surface. *Earth and Planetary Science Letters* **413**, 1–12.

1133 Muir, R. J., Weaver, S. D., Bradshaw, J. D., Eby, G. N. & Evans, J. A. (1995). The Cretaceous
1134 Separation Point batholith, New Zealand: granitoid magmas formed by melting of
1135 mafic lithosphere. *Journal of the Geological Society* **152**, 689–701.

1136 Neave, D. A., Buisman, I. & Maclennan, J. (2017). Continuous mush disaggregation during
1137 the long-lasting Laki fissure eruption, Iceland. *American Mineralogist* **102**, 2007–
1138 2021.

1139 Nicholls, J. & Stout, M. Z. (1997). Epitactic overgrowths and intergrowths of clinopyroxene
1140 on orthopyroxene; implications for paths of crystallization, 1881 lava flow, Mauna
1141 Loa Volcano, Hawaii. *The Canadian Mineralogist* **35**, 909–922.

Paterson, S. R., Vernon, R. H. & Zak, J. (2005). Mechanical Instabilities and Physical Accumulation of K-feldspar Megacrysts in Granitic Magma, Tuolumne Batholith, California, USA. *Journal of the Virtual Explorer* **18**.

Peres, S., Griffiths, T. A., Colle, F., Lelarge, S. I., Masotta, M., Pontesilli, A., Mancini, L. & Abart, R. (2024). Identifying crystal nucleation mechanisms in a synthetic trachybasalt: a multimodal approach. *Contributions to Mineralogy and Petrology* **179**, 84.

Schuster, R., Tiede, L., Ageeva, O., Griffiths, T. A., Abart, R. & Habler, G. (2023). Microstructure and Texture of a Spinel Corona Around a Basalt Hosted Corundum Xenocrystal. *Journal of Petrology* **64**, egac130.

Schwindinger, K. R. (1999). Particle dynamics and aggregation of crystals in a magma chamber with application to Kilauea Iki olivines. *Journal of Volcanology and Geothermal Research* **88**, 209–238.

Schwindinger, K. R. & Anderson, A. T. (1989). Synneusis of Kilauea Iki olivines. *Contributions to Mineralogy and Petrology* **103**, 187–198.

Słaby, E., Galbarczyk-Gąsiorowska, L., Seltmann, R. & Müller, A. (2007). Alkali feldspar megacryst growth: Geochemical modelling. *Mineralogy and Petrology* **89**, 1–29.

Tarney, J. (1969). Epitaxic relations between coexisting pyroxenes. *Mineralogical Magazine* **37**, 115–122.

Vance, J. A. (1969). On synneusis. *Contributions to Mineralogy and Petrology* **24**, 7–29.

Vernon, R. H. (1986). K-feldspar megacrysts in granites — Phenocrysts, not porphyroblasts. *Earth-Science Reviews* **23**, 1–63.

Vernon, R. H. (2016). Rapakivi granite problems: plagioclase mantles and ovoid megacrysts. *Australian Journal of Earth Sciences* **63**, 675–700.

Vernon, R. H. (2018). *A Practical Guide to Rock Microstructure*. Cambridge University Press.

Vernon, R. H. & Paterson, S. R. (2008). How late are K-feldspar megacrysts in granites? *Lithos* **104**, 327–336.

Vogt, J. H. L. (1921). The Physical Chemistry of the Crystallization and Magmatic Differentiation of Igneous Rocks. *The Journal of Geology* **29**, 318–350.

Welsch, B., Faure, F., Famin, V., Baronnet, A. & Bachèlery, P. (2013). Dendritic Crystallization: A Single Process for all the Textures of Olivine in Basalts? *Journal of Petrology* **54**, 539–574.

Whitney, J. A. (1988). The origin of granite: The role and source of water in the evolution of granitic magmas. *Geological Society of America Bulletin* **100**, 1886–1897.

1177 Wieser, P. E., Vukmanovic, Z., Kilian, R., Ringe, E., Holness, M. B., Maclennan, J. &
1178 Edmonds, M. (2019). To sink, swim, twin, or nucleate: A critical appraisal of crystal
1179 aggregation processes. *Geology* **47**, 948–952.

1180 Yemmou, M., Brierre, A. & Azouni, M. A. (1991). Rejection and capture of solid particles by
1181 ice. *Advances in Space Research* **11**, 327–330.

1182

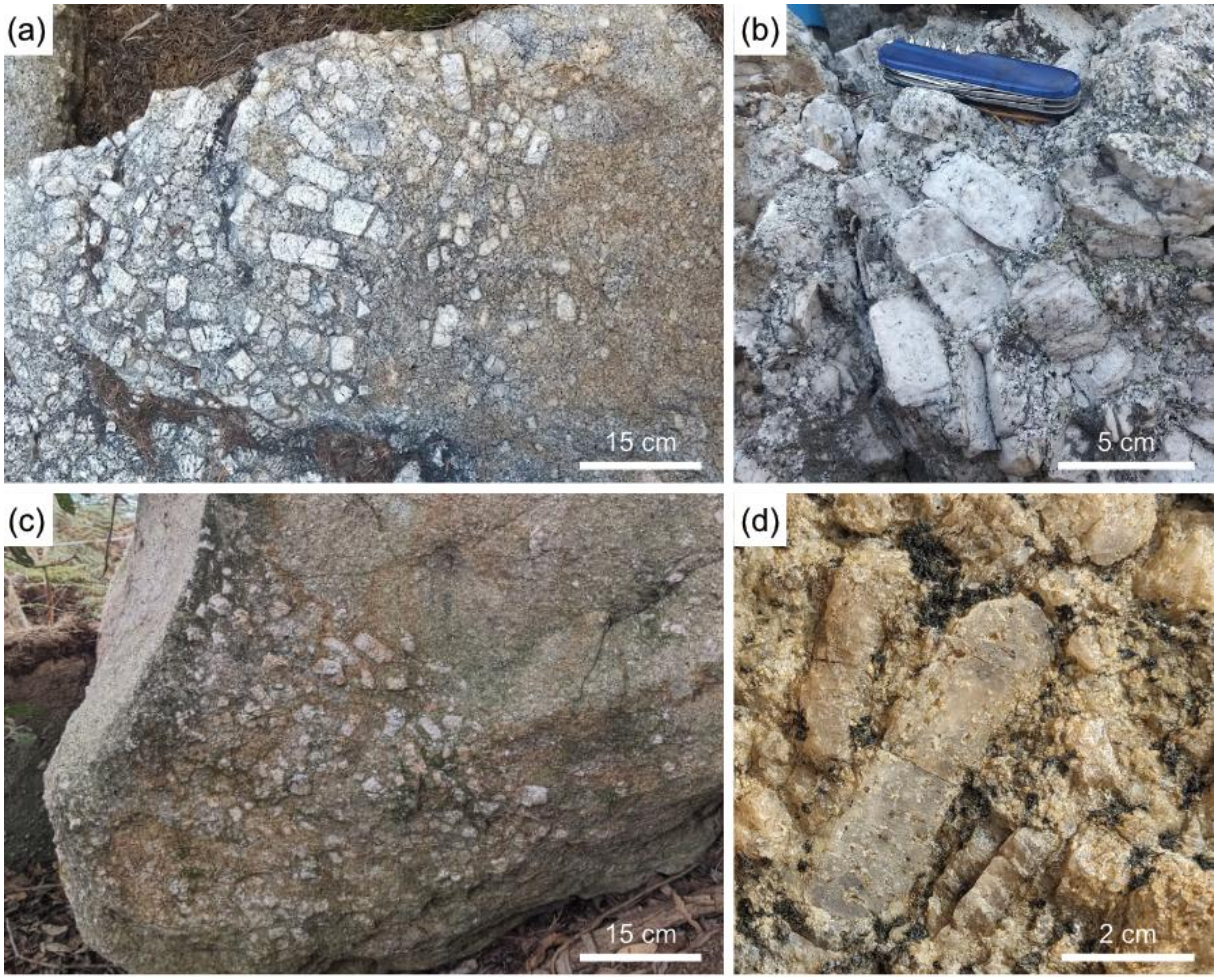

Figure 1: Field photographs of megacrysts in (a, b) Tuolumne Cathedral Peak Granodiorite and (c, d) Separation Point Granite.

Table 1: Sampling localities and EBSD data collection information.

Sample	Pluton	Grid reference (NAD 83)	SEM used for EBSD	EBSD step size
B	pHD	283641 4190262	Zeiss	15 µm
D	pHD/CP contact	284877 4191708	Zeiss	15 µm
G	CP	286173 4193621	Zeiss	20 µm
I	CP	289246 4195221	Zeiss	15 µm
SP2	SP	N/A	Quanta	13 µm

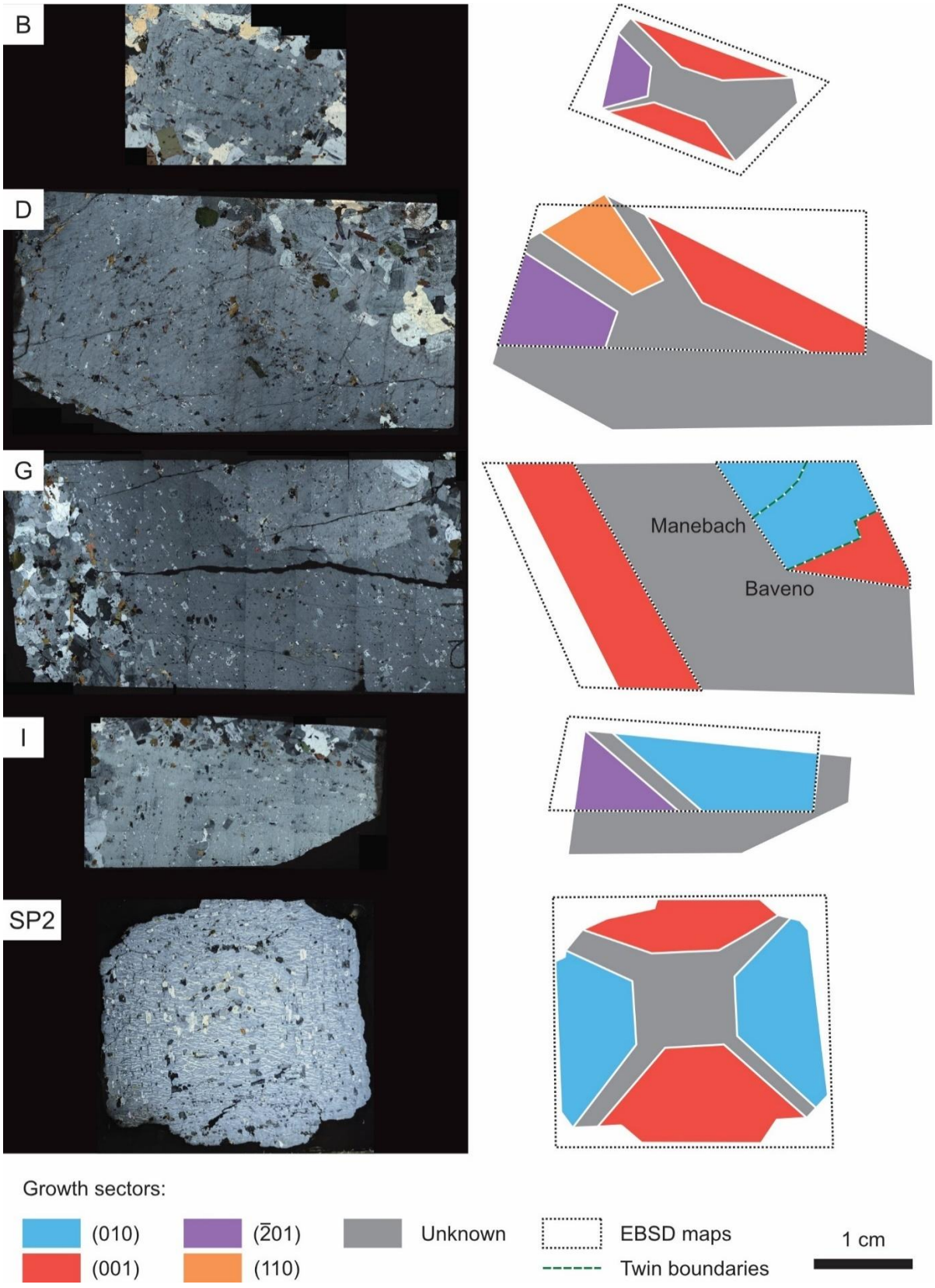

Figure 2: Transmitted light maps (left) and sketches (right) of each of the analysed megacrysts. B, D, G and I are imaged with circularly polarised light; SP2 is imaged with

cross-polarised light. Sketches represent only the euhedral portions of the megacrysts, with the growth sectors colour coded and the EBSD map locations marked.

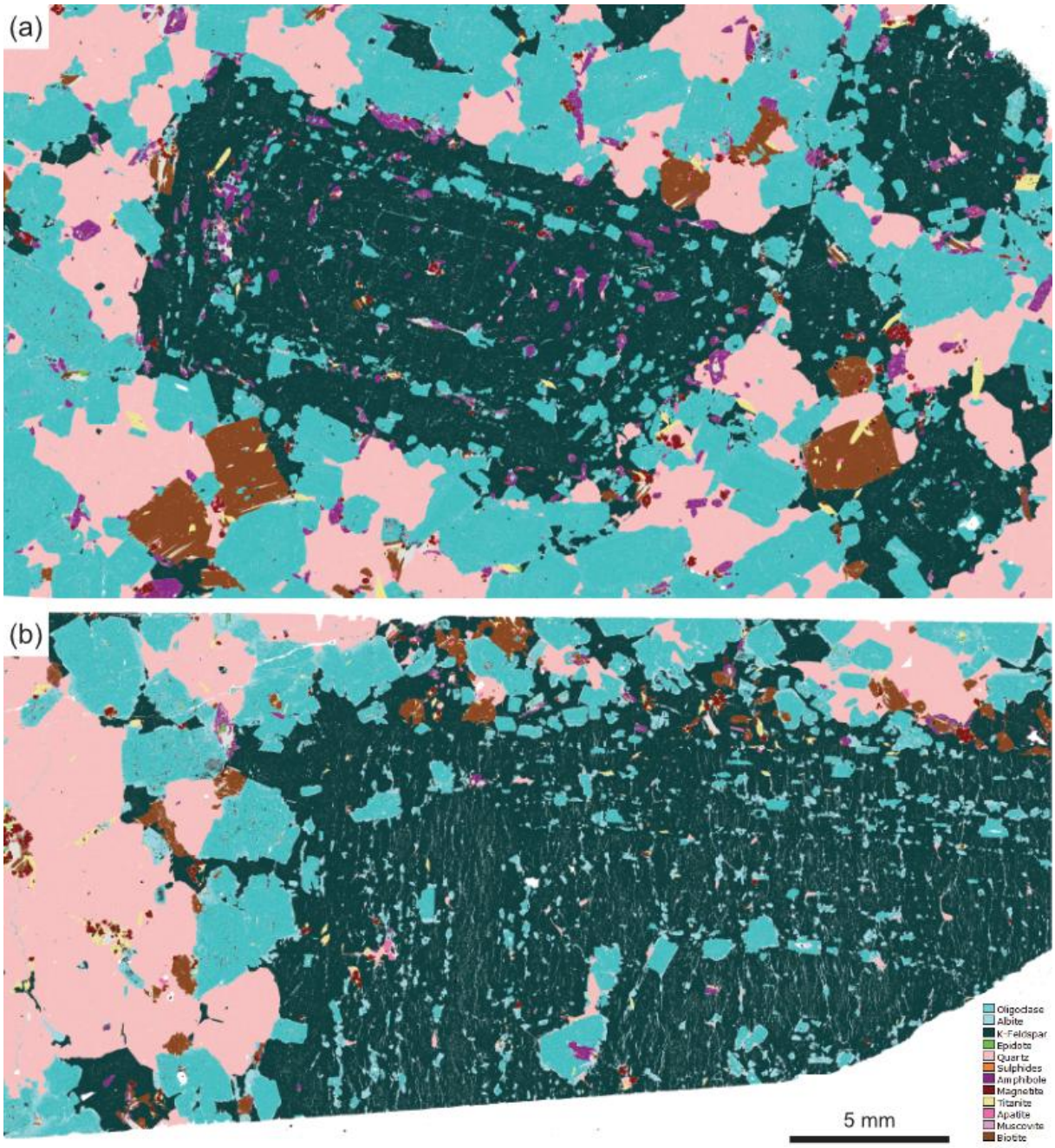

Figure 3: Phase maps of (a) sample B and (b) sample I, showing inclusion distributions.

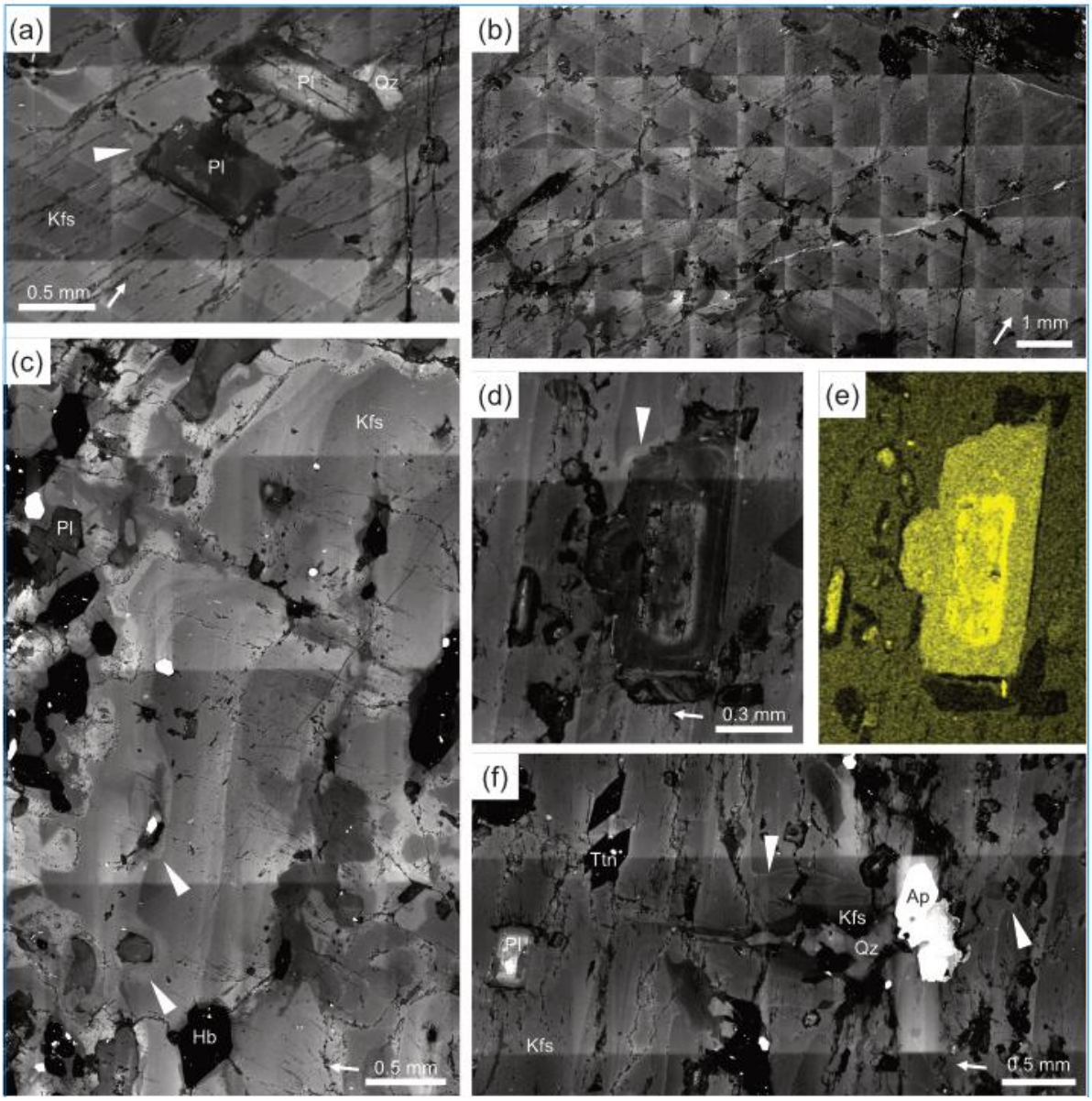

Figure 4: CL images of the megacrysts and their inclusions. Arrows next to scale bars point in the megacryst growth direction. (a) Zoned plagioclase inclusions (shallow embayment arrowed). (b) Typical relatively planar euhedral zones in a megacryst. (c) Resorbed boundaries, including embayments around inclusions (arrowed) and truncation of previous zones (e.g., top right). (d) Zoned plagioclase inclusion with an embayment following its boundary (arrowed) and (e) an EDS calcium map of the same inclusion showing its more calcic core. (f) A deep embayment (arrowed, centre) with a quartz core. Other shallow embayments (example arrowed on right) are also present around plagioclase inclusion grain boundaries.

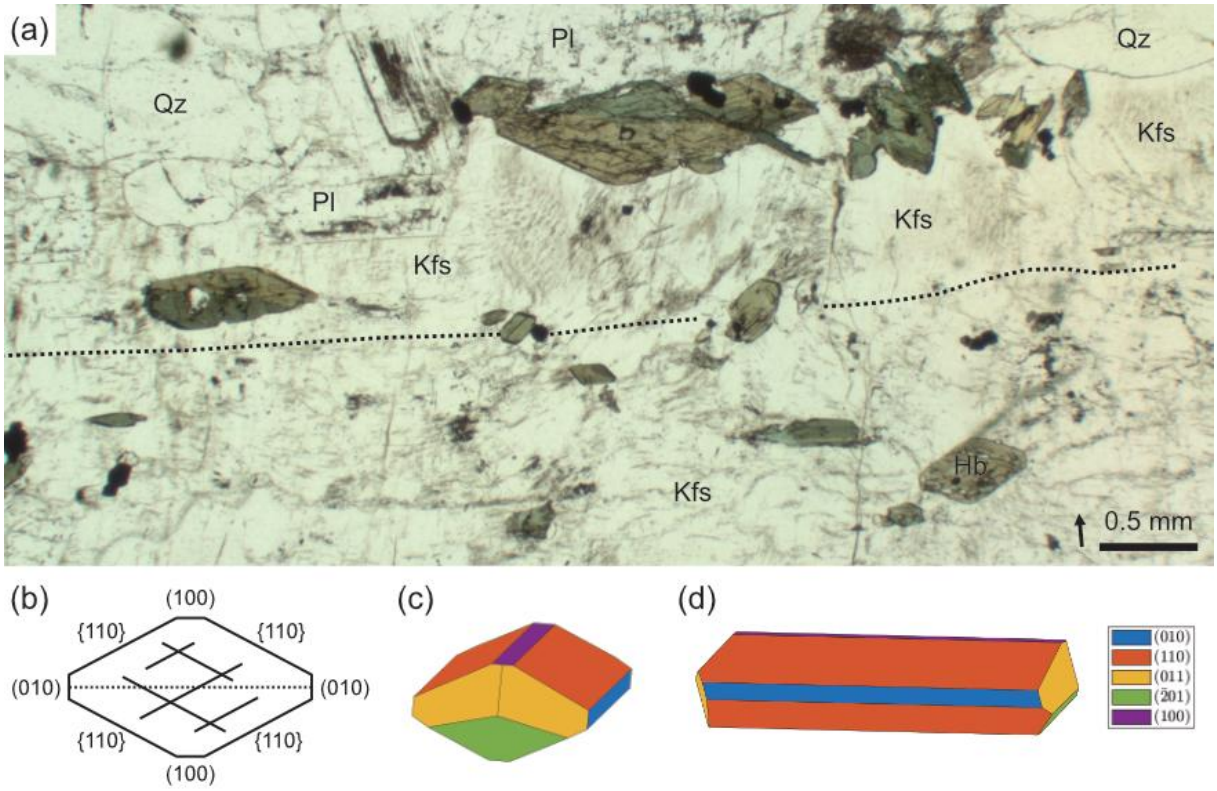

Figure 5: (a) Typical amphibole inclusions (green) in Sample B from pHD. The dashed line marks the outermost major zone boundary visible in CL in the megacryst and the arrow next to the scale bar indicates the growth direction of the megacryst. (b) Schematic cross-section of a typical amphibole looking down [001]. The dashed line is the typical twin plane, (100). {110} cleavages are indicated schematically. Also shown are 3D models of amphibole habits similar to those found in the Tuolumne samples, both (c) looking approximately down [001] and (d) looking approximately down [010] to show elongation along [001].

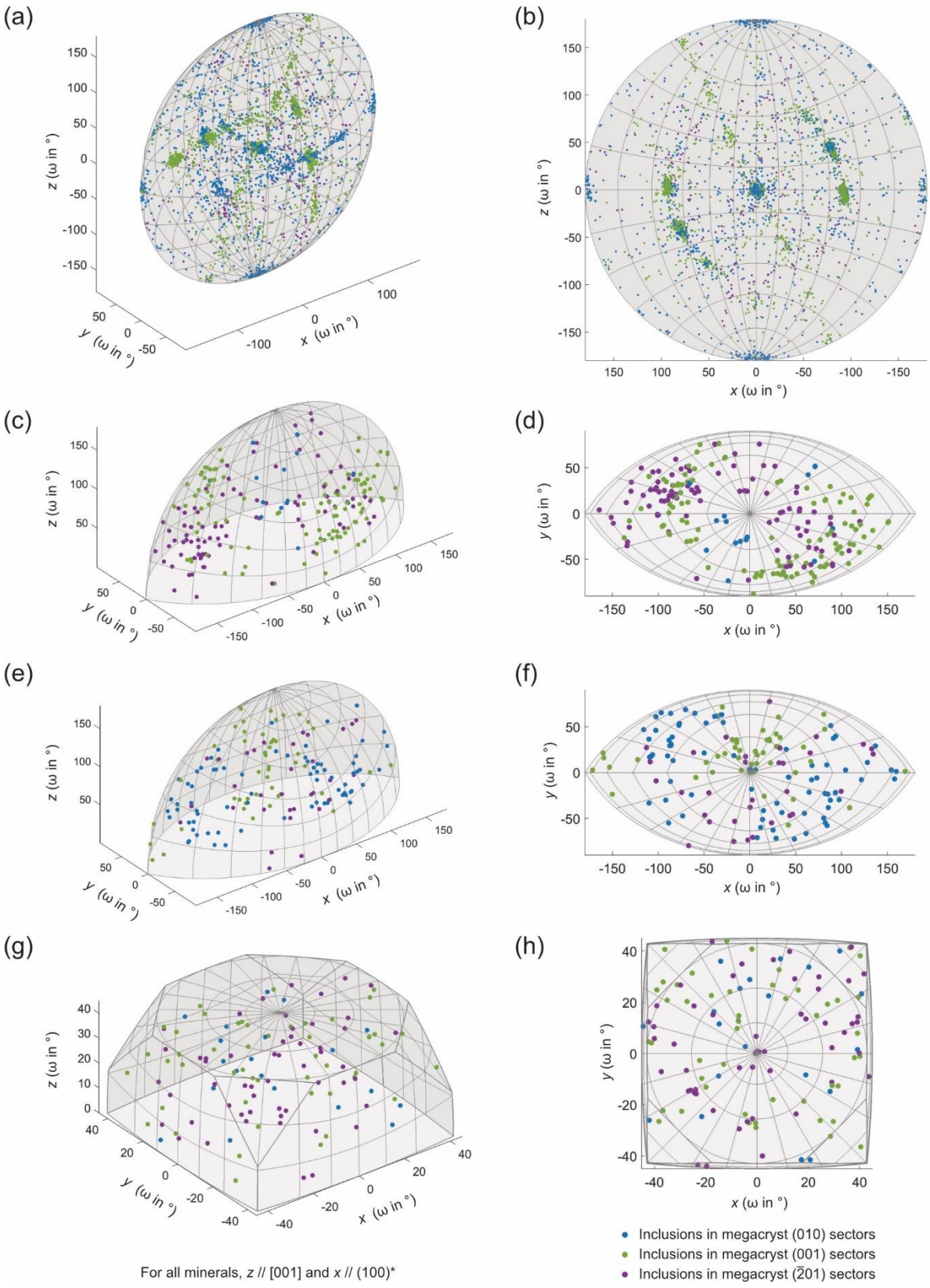

Figure 6: 3D axis-angle plots of the misorientation data between K-feldspar and each inclusion mineral, with fundamental regions shown in light grey and data points coloured by

the megacryst growth sector in which each inclusion is located. ω is misorientation angle. For each plot, an oblique view (left) and a view projected along one axis (right) are shown. (a, b) plagioclase; (c, d) amphibole; (e, f) titanite; (g, h) magnetite.

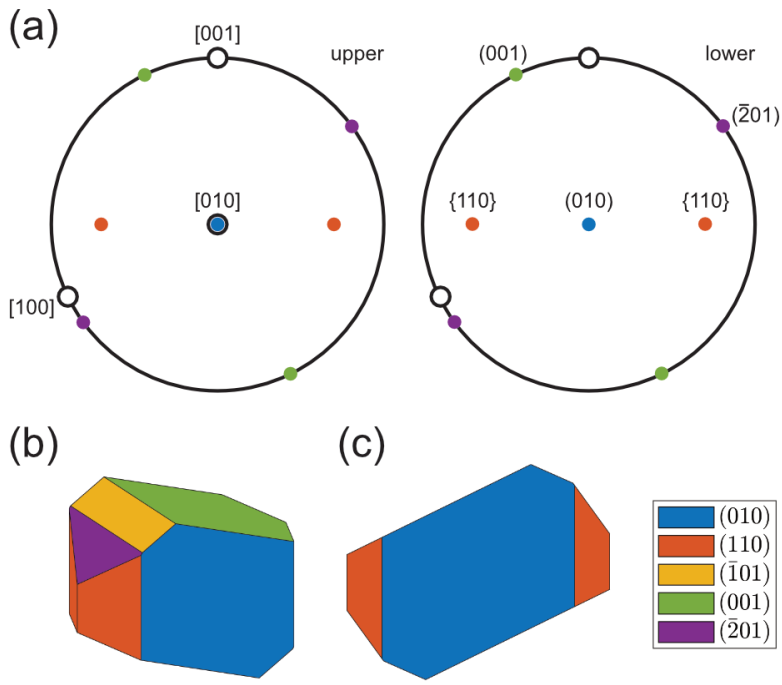

Figure 7: The megacryst reference frame into which the inclusion data were rotated. (a) Pole figure of the K-feldspar axes (labelled in the upper hemisphere) and main planes (labelled in the lower hemisphere). (c) Schematic K-feldspar habit in an arbitrary orientation, showing the main faces. (d) K-feldspar in the reference orientation.

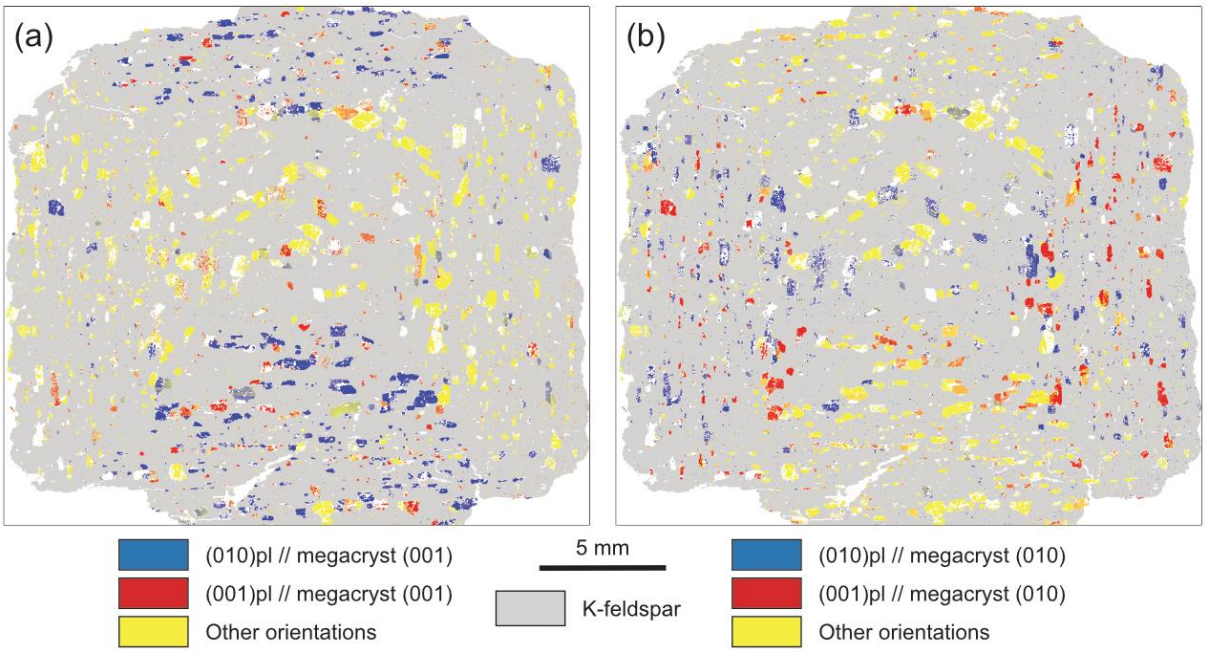

Figure 8: EBSD map of SP2 showing plagioclase coloured by its orientation relationship to the host K-feldspar crystal (in grey), illustrating that plagioclase orientations are arranged in sectors defined by the growth faces of the megacryst. (a) Plagioclase coloured relative to $(001)_{Kfs}$ which are the top and bottom megacryst faces in this map. (b) Plagioclase coloured relative to $(010)_{Kfs}$ which are the side faces in this map (see also Fig. 2).

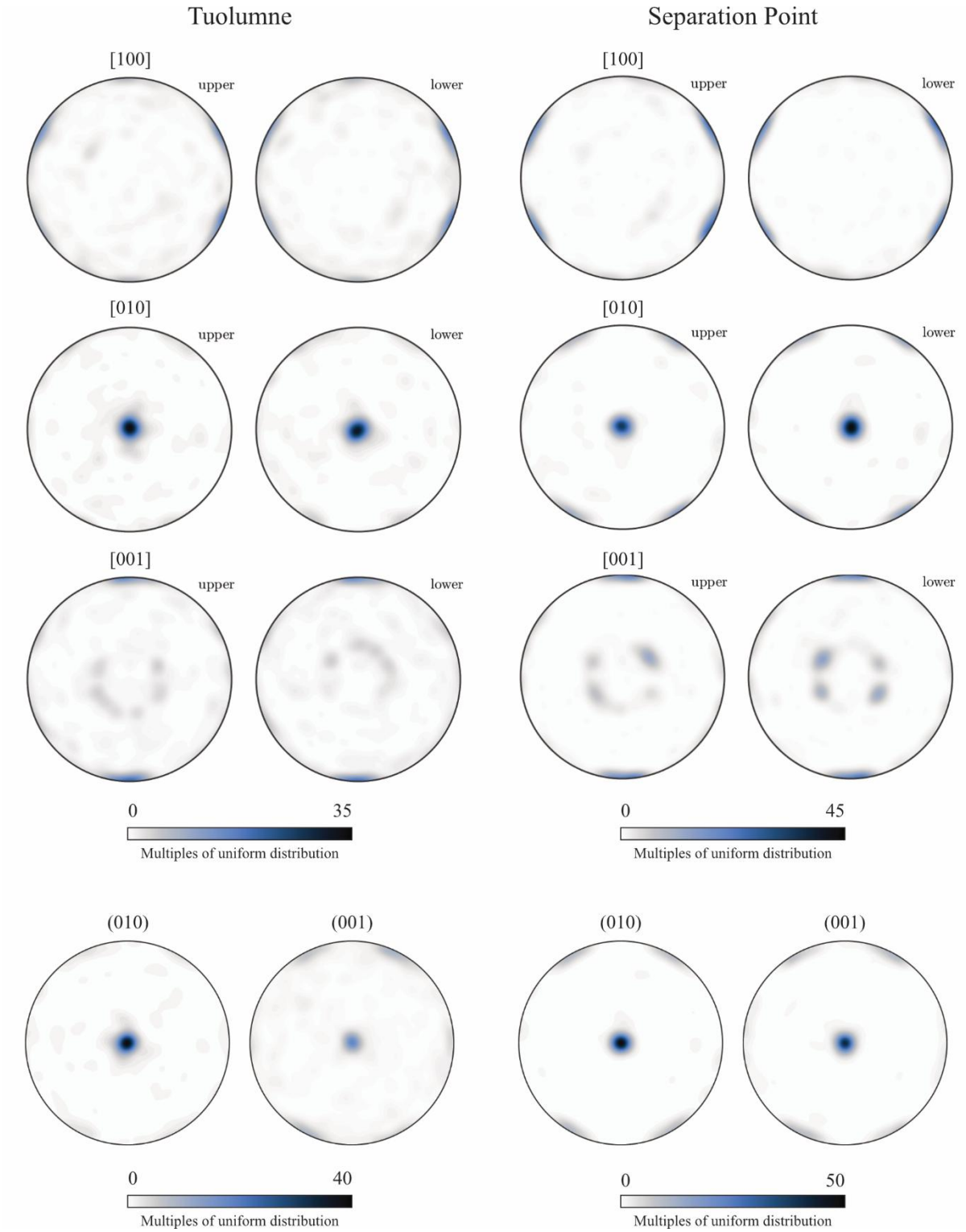

Figure 9: Pole figures of data from plagioclase inclusions in the $(010)_{Kfs}$ growth sectors of megacrysts from Tuolumne (left, n = 742) and Separation Point (right, n = 653) plotted in the K-feldspar reference frame (Fig. 7). We plot both hemispheres for the axes $[100]_{Pl}$, $[010]_{Pl}$ and $[001]_{Pl}$, and the lower hemisphere for poles to the $(010)_{Pl}$ and $(001)_{Pl}$ planes.

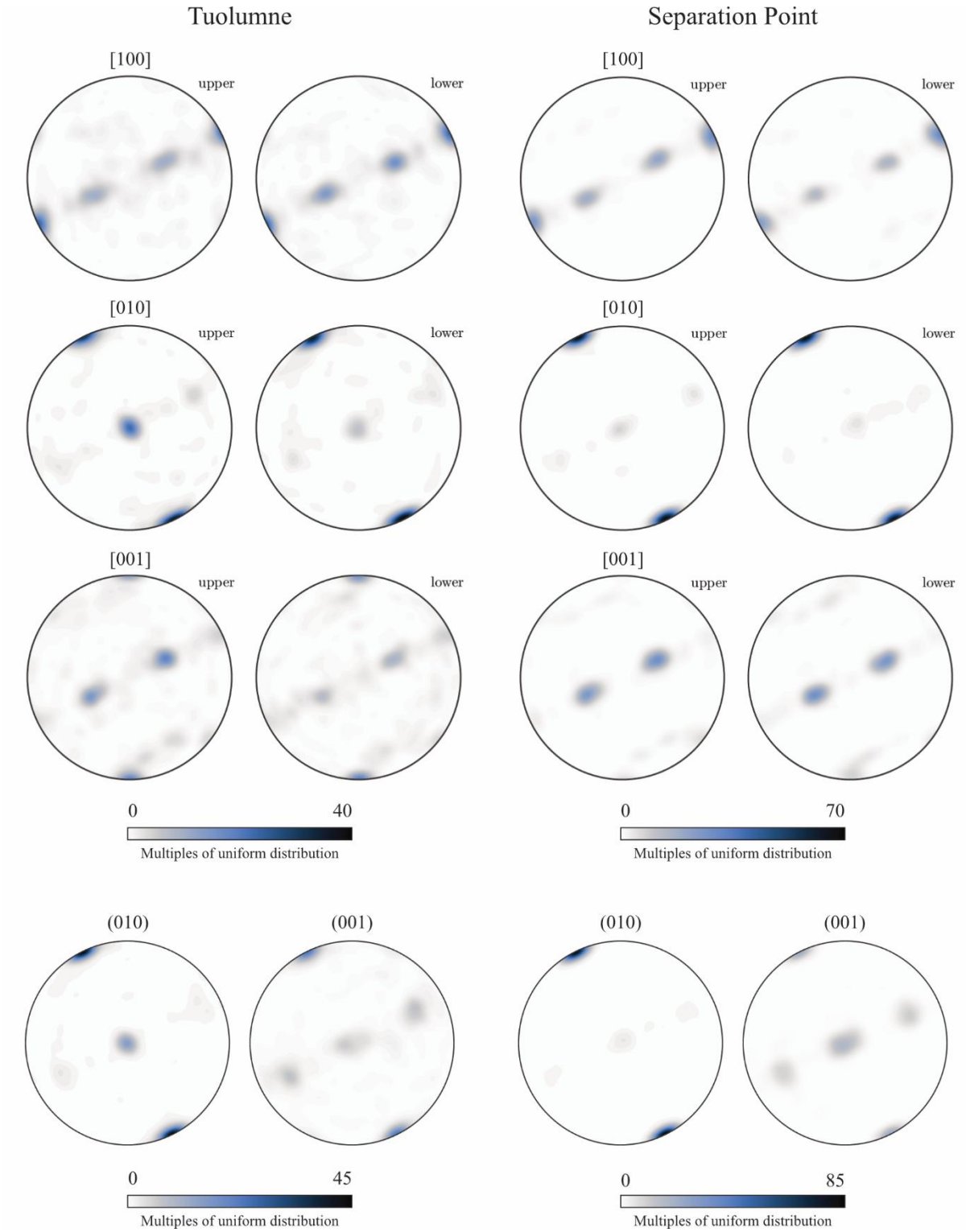

Figure 10: Pole figures of data from plagioclase inclusions in the (001) growth sectors of megacrysts from Tuolumne (left, n = 758) and Separation Point (right, n = 665) plotted in the K-feldspar reference frame (Fig. 7). We plot both hemispheres for the axes $[100]_{Pl}$, $[010]_{Pl}$ and $[001]_{Pl}$, and the lower hemisphere for poles to the $(010)_{Pl}$ and $(001)_{Pl}$ planes.

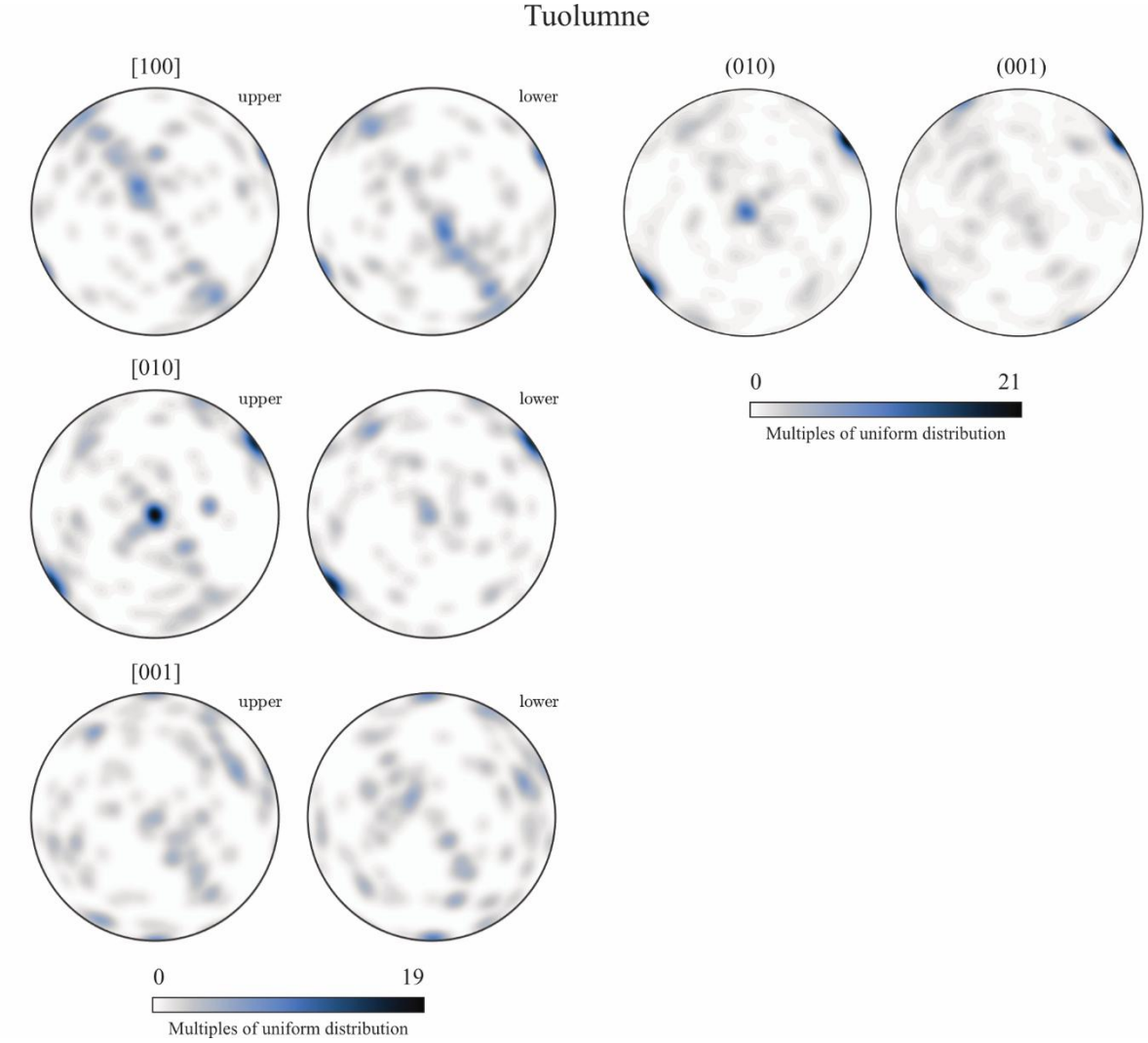

Figure 11: Pole figures of data from plagioclase inclusions in the $(\bar{2}01)_{Kfs}$ growth sectors of megacrysts from Tuolumne (n = 294) plotted in the K-feldspar reference frame (Fig. 7). No data were collected from Separation Point. We plot both hemispheres for the axes $[100]_{Pl}$, $[010]_{Pl}$ and $[001]_{Pl}$, and the lower hemisphere for poles to the $(010)_{Pl}$ and $(001)_{Pl}$ planes.

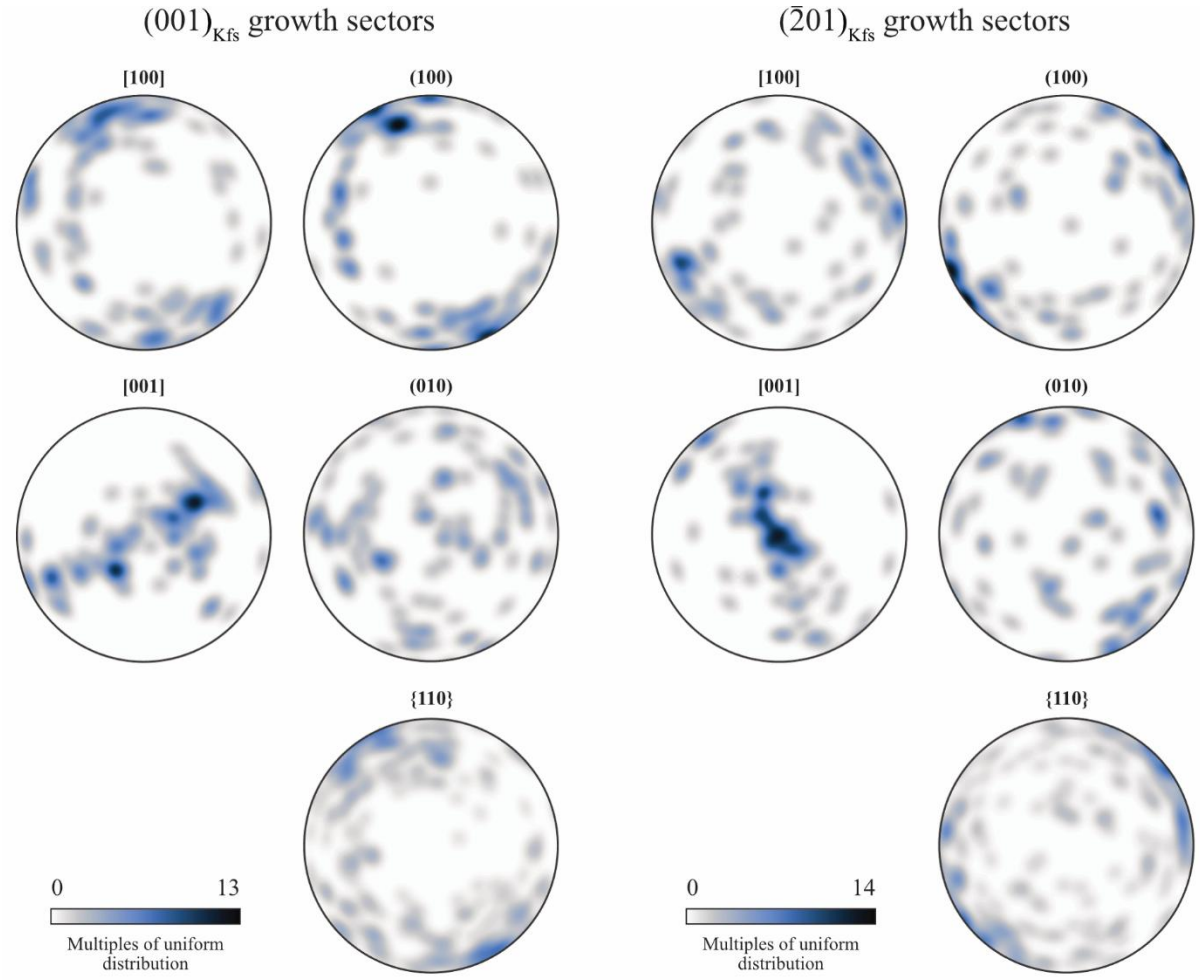

Figure 12: Lower hemisphere pole figures of amphibole inclusions in the $(001)_{Kfs}$ growth sectors (left, n = 105) and the $(\bar{2}01)_{Kfs}$ growth sectors (right, n = 90) of megacrysts from Tuolumne plotted in the K-feldspar reference frame (Fig. 7).

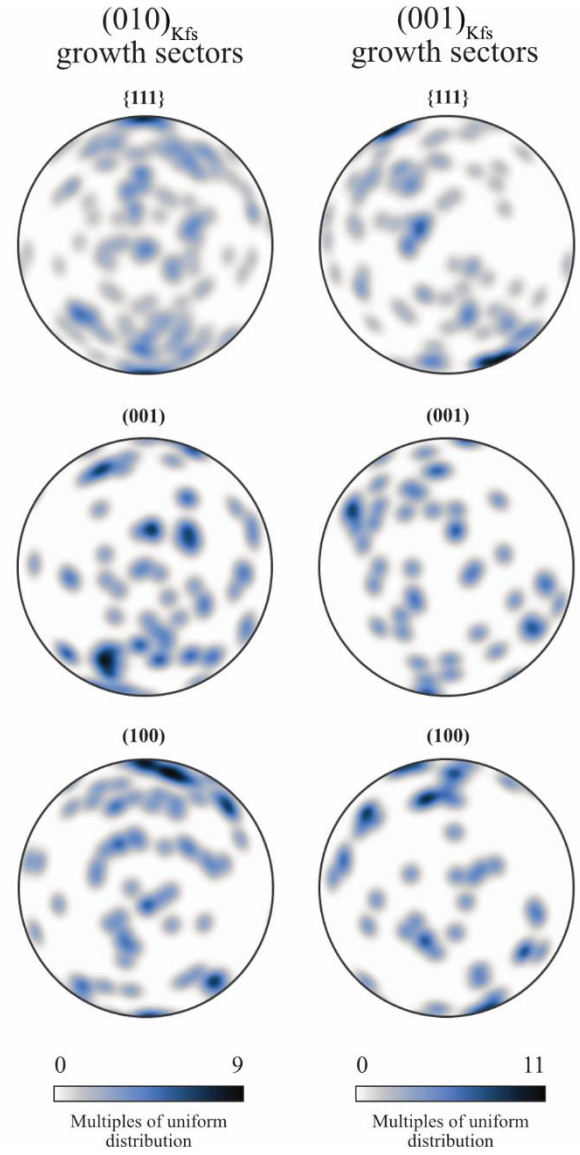

Figure 13: Lower hemisphere pole figures of titanite inclusions in the $(010)_{Kfs}$ growth sectors (left, $n = 73$) and the $(001)_{Kfs}$ growth sectors (right, $n = 49$) of megacrysts from Tuolumne and SP, plotted in the K-feldspar reference frame (Fig. 7). Titanite Miller indices are in the morphological unit cell.

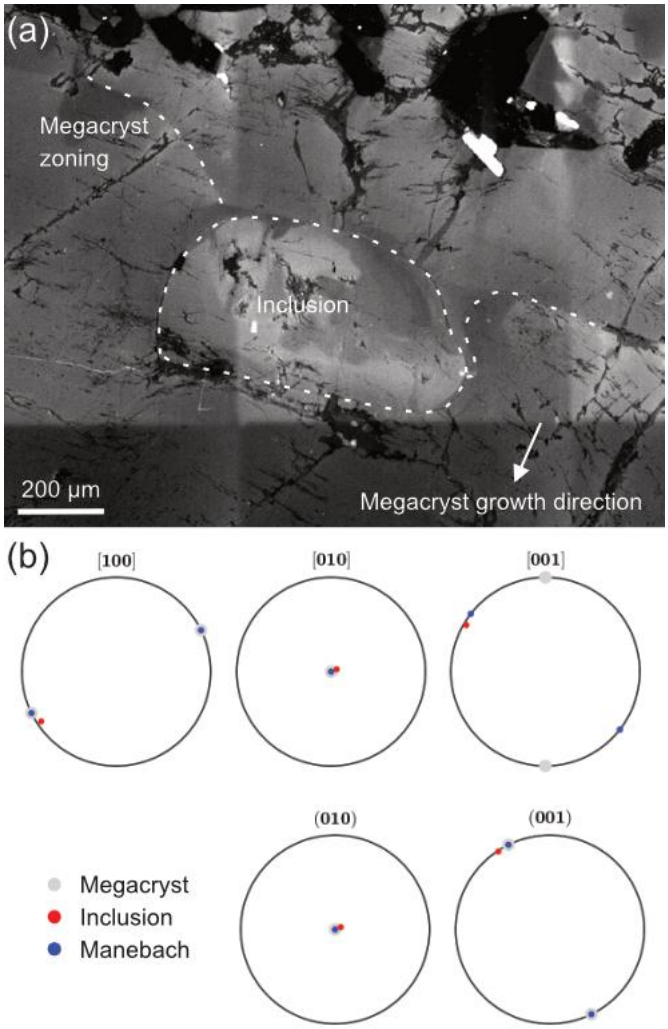

Figure 14: (a) CL map of a K-feldspar inclusion. Dashed lines indicate the megacryst compositional zoning, and the inclusion boundary. (b) Pole figures of the host crystal, inclusion, and an idealised Manebach twin (plotted in the standard reference frame, not the reference frame of the image).

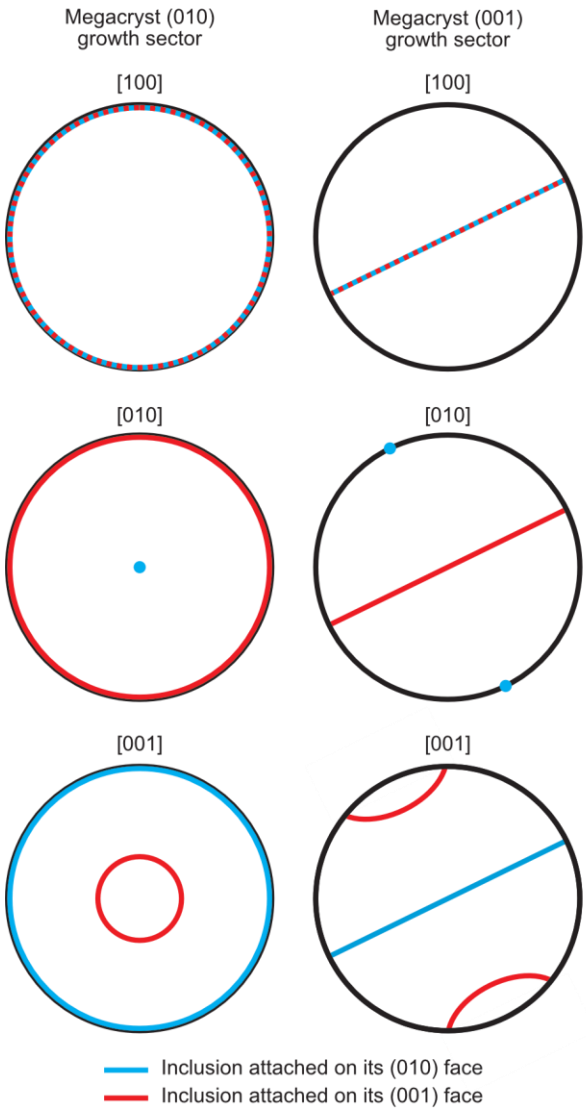

Figure 15: Modelled pole figures illustrating the expected distributions of plagioclase axes in (left) the (010) growth sectors of the megacryst and (right) the (001) growth sectors if the only controlling factor were attachment on (010) and (001).

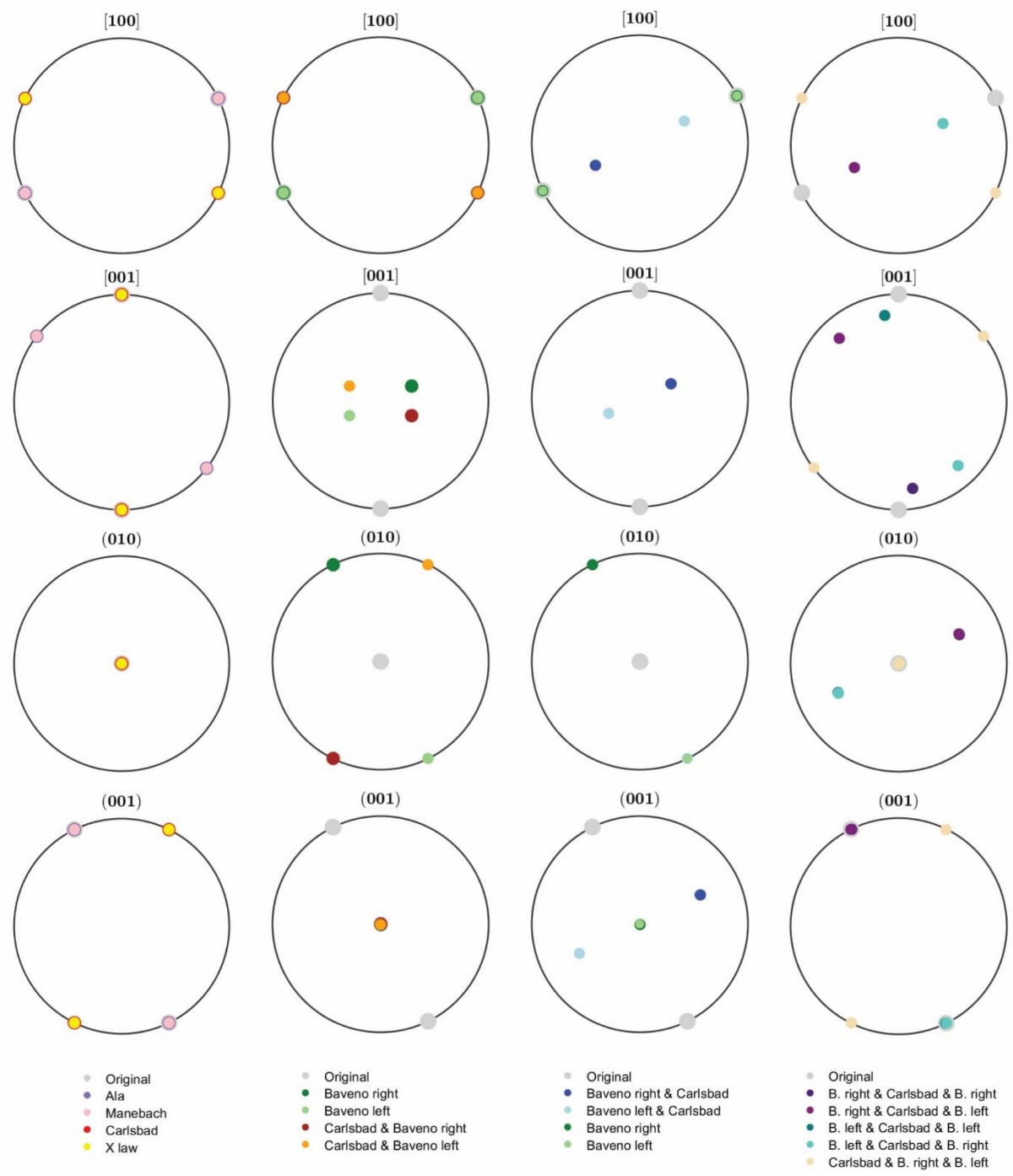

Figure 16: Modelled twin and twin combination relationships for monoclinic feldspars, relative to the megacryst reference frame (light grey) with antipodal projection onto a single hemisphere. Results are grouped into four columns to reduce overlapping of points.

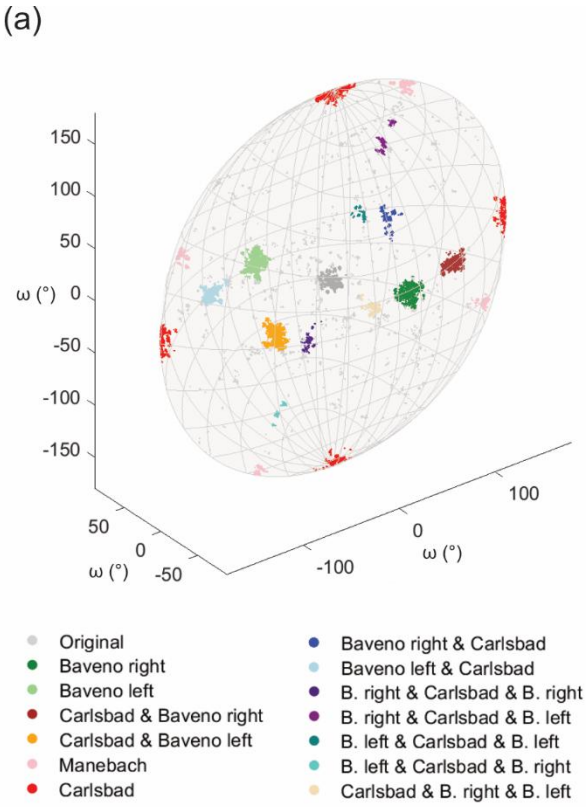

Figure 17: (a) Summary axis-angle plot showing the plagioclase inclusion data from sample SP2 coloured by orientation relationship to the host. (b) Schematic diagram of the observed synneusis relationships between K-feldspar (large) and plagioclase (small). Inclusions, coloured by synneusis relationship, are pictured on the host faces on to which they attach.